



**HAL**  
open science

# Understanding the Role of Rainfall and Hydrology in Determining Fluvial Erosion Efficiency

E. Deal, J. Braun, G. Botter

► **To cite this version:**

E. Deal, J. Braun, G. Botter. Understanding the Role of Rainfall and Hydrology in Determining Fluvial Erosion Efficiency. *Journal of Geophysical Research: Earth Surface*, 2018, 123, pp.744-778. 10.1002/2017JF004393 . insu-03595912

**HAL Id: insu-03595912**

**<https://insu.hal.science/insu-03595912>**

Submitted on 3 Mar 2022

**HAL** is a multi-disciplinary open access archive for the deposit and dissemination of scientific research documents, whether they are published or not. The documents may come from teaching and research institutions in France or abroad, or from public or private research centers.

L'archive ouverte pluridisciplinaire **HAL**, est destinée au dépôt et à la diffusion de documents scientifiques de niveau recherche, publiés ou non, émanant des établissements d'enseignement et de recherche français ou étrangers, des laboratoires publics ou privés.

Copyright

## RESEARCH ARTICLE

10.1002/2017JF004393

## Understanding the Role of Rainfall and Hydrology in Determining Fluvial Erosion Efficiency

## Key Points:

- Integration of hydrology into a stream power model yields new insight into climatic controls on fluvial erosion efficiency
- The nonlinearity between the steepness index and erosion rate is controlled by erosion thresholds, hydroclimatic conditions, and channel hydraulics
- Hydrology influences how erosive a particular climate forcing will be

## Correspondence to:

E. Deal,  
ericdeal@mit.edu

## Citation:

Deal, E., Braun, J., & Botter, G. (2018). Understanding the role of rainfall and hydrology in determining fluvial erosion efficiency. *Journal of Geophysical Research: Earth Surface*, 123, 744–778. <https://doi.org/10.1002/2017JF004393>

Received 18 JUN 2017

Accepted 12 FEB 2018

Accepted article online 17 FEB 2018

Published online 26 APR 2018

E. Deal<sup>1,2,3</sup> , J. Braun<sup>1,2,4</sup>, and G. Botter<sup>5</sup> 

<sup>1</sup>Institut des Sciences de la Terre, Université Grenoble-Alpes, Saint-Martin-d'Hères, France, <sup>2</sup>Helmholtz Centre Potsdam, GFZ German Research Center for Geosciences, Potsdam, Germany, <sup>3</sup>Currently at Earth, Atmospheric and Planetary Sciences, Massachusetts Institute of Technology, Cambridge, MA, USA, <sup>4</sup>University of Potsdam, Potsdam, Germany, <sup>5</sup>Department of Civil, Architectural and Environmental Engineering (ICEA), University of Padova, Padova, Italy

**Abstract** Due to the challenges in upscaling daily climatic forcing to geological time, physically realistic models describing how rainfall drives fluvial erosion are lacking. To bridge this gap between short-term hydrology and long-term geomorphology, we derive a theoretical framework for long-term fluvial erosion rates driven by realistic climate by integrating an established stochastic-mechanistic model of hydrology into a threshold-stochastic formulation of stream power. The hydrological theory provides equations for the daily streamflow probability distribution as a function of climatic boundary conditions. The new parameters introduced are rooted firmly in established climatic and hydrological theory. This allows us to account for how fluvial erosion rates respond to changes in rainfall intensity, frequency, evapotranspiration rates, and soil moisture dynamics in a way that is consistent with existing theories. We use this framework to demonstrate how hydroclimatic conditions and erosion threshold magnitude control the degree of nonlinearity between steepness index and erosion rate. We find that hydrological processes can have a significant influence on how erosive a particular climatic forcing will be. By accounting for the influence of hydrology on fluvial erosion, we conclude that climate is an important control on erosion rates and long-term landscape evolution.

## 1. Introduction

Rivers play an important role in shaping Earth's surface, especially in high relief, mountain environments; they have become a major focus of research in quantitative geomorphology (e.g., Tucker & Hancock, 2010; Whipple et al., 1999, 2009), because they are one of the main links between climate and erosion (e.g., Burbank et al., 2003; Crave & Davy, 2001; DiBiase & Whipple, 2011; DiBiase et al., 2010; Lague, 2014; Tucker & Bras, 2000; Whipple & Tucker, 1999). Mountainous bedrock rivers control landscape evolution in unglaciated mountain environments by steepening hillslopes through bedrock incision and transporting away the resulting debris. In doing so, they not only set the relief structure of mountainous regions but also communicate tectonic signals throughout the landscape (Whipple, 2009; Whipple et al., 1999). All of this is accomplished ultimately by the ability of flowing water to transport sediment. Therefore, it is natural to conclude that climate, or more specifically, rainfall, plays an important role in landscape evolution as the main source of water. Gilbert (1877) pointed this out more than 140 years ago. In the intervening time there have been myriad theoretical models postulating, and sometimes demonstrating, that climate should play an integral part in determining the form and rate of change of Earth's surface. Some consider climate specifically in the context of a landscape dominated by fluvial erosion (e.g., Beaumont et al., 1992; Roe et al., 2002; Whipple et al., 1999), and others in a more general sense (e.g., Dahlen & Suppe, 1988; Willett, 1999; Whipple & Meade, 2006).

Despite theoretical predictions and the obvious influence of rainfall on erosion processes at the local scale, many studies attempting to relate mean rainfall rates or stream power to erosion rates struggle to find a functional relationship across a range of spatial and temporal scales (e.g., Acosta et al., 2015; Bermudez et al., 2012; Blanckenburg, 2005; Burbank et al., 2003; Godard et al., 2014; Riebe et al., 2001). However, a few studies that carefully consider factors that may obscure the relationship between rainfall and erosion rates find a clearer relationship (e.g., Ferrier et al., 2013). This suggests that when the major confounding factors can be tightly controlled, a relationship between climate and erosion can emerge. In a fluvially dominated landscape, some of these factors include spatially varying rock type and uplift rate, erosion thresholds, the intensity

and frequency of significant storms, the kind and amount of vegetation, sediment supply and transport dynamics, channel form, and likely other as yet unidentified factors. In order to implement a landscape evolution model that incorporates realistic climatic forcing, these confounding factors must be elucidated and accounted for, and their potential effect on erosional efficiency must be quantified.

A major difficulty with understanding the impact of climate on fluvial erosion is the large disparity in timescales. Rainfall rates relevant to erosion processes and streamflow generation vary over hours to days, whereas the timescales relevant to landscape evolution rates are centuries to millennia. The ecological and hydrological responses to climatic forcing are also time dependent, complex, and have a nontrivial influence on landscape evolution (Istanbulluoglu, 2009). It is a challenge to establish geomorphic transport laws that capture the net effects of this complexity over the relevant ranges of spatial and temporal scales in a quantifiable way. Initial attempts used a parameterized effective streamflow that was assumed to capture the average effect of sediment-laden water flowing over bedrock (Beaumont et al., 1992; Tucker & Slingerland, 1994; Wolman & Miller, 1960). However, it is well known that there exist thresholds for fluvial transport and erosion (e.g., Bagnold, 1980; Baker & Kale, 1998; Howard, 1994; Shields, 1936). It has been repeatedly shown that in the presence of thresholds, as well as other nonlinearities between streamflow and fluvial erosion, effective streamflow approaches are unsuitable (Lague et al., 2005; Snyder et al., 2003; Tucker & Bras, 2000).

Stochastic treatments are well suited to the task of understanding the long-term effect of nonlinear time and state-dependent processes operating over short timescales and thus provide an opportunity for linking climatic and fluvial erosion processes. Pioneering efforts by Tucker and Bras (2000), Crave and Davy (2001), Snyder et al. (2003), and Lague et al. (2005) using stochastic rainfall forcing and/or the full probability distribution of streamflow demonstrated the necessity of using a threshold-stochastic approach rather than a constant effective streamflow one. These studies established a theoretical basis for the use of streamflow variability in landscape evolution models, a concept long considered important (e.g., Wolman & Miller, 1960). Recent work has shown that these stochastic models predict catchment-scale erosion rates relatively well (Scherler et al., 2017). While these studies have done much to account for the temporal complexities inherent in rainfall and streamflow, they have not managed to connect rainfall to streamflow in a convincing way. Crave and Davy (2001), Tucker (2004), and Tucker and Bras (2000) used a simplified model for hydrology which is only applicable in small catchments (tens of km<sup>2</sup>). Lague et al. (2005) made use of an inverse gamma distribution of daily streamflow known to match natural hydrological systems well but did not include any model for hydrology itself. Ijjász-Vásquez et al. (1992) developed a clever way to integrate stochastic rainfall into a hydrological and landscape evolution model, but the hydrological model used is ultimately a constant effective streamflow one. Several other studies have relied on simplified hydrologic models similar to Tucker and Bras (2000) (e.g., Collins et al., 2004; Istanbulluoglu & Bras, 2006).

In order to explore how climate influences fluvial landscape evolution, it is critical that some of the complexity of hydrological systems be modeled, so that river streamflow can respond realistically to changing climatic and hydrological conditions. For example, it has been observed that the transformation of rainfall to streamflow is nonlinear, with heavy-tailed probability distributions of streamflow resulting from light-tailed rainfall distributions (Basso, Schirmer, & Botter, 2015; Rossi et al., 2016), which has important implications for fluvial erosion. In addition, there are other aspects of landscapes besides rainfall that determine the fluvial response to a particular climatic forcing, such as vegetation (mainly through evapotranspiration), dynamics of soil moisture storage, as well as how and how fast water is transmitted through basins to rivers (Huang & Niemann, 2008; Istanbulluoglu, 2009; Rodriguez-Iturbe, 2000; Rossi et al., 2016).

Landscape evolution models that include hydrology in varying degrees of complexity exist. For example, Huang and Niemann (2006a) and Huang and Niemann (2008) present landscape evolution models with a sophisticated hydrological component. However, they require very short time steps that make the models slow to run (runtimes measured in weeks). More modern, but similar models still require weeks to run (Zhang et al., 2016). Using the Channel-Hillslope Integrated Landscape Development framework (Tucker et al., 2001), Yetemen et al. (2015) develop a landscape evolution model with a sophisticated vegetation growth and water use component, but again, the model is restricted to daily time steps. Realism and accuracy must be balanced with computational efficiency and generality. A landscape evolution model that requires extensive calibration or time steps on the order of hours or days to keep track of ecological and hydrological processes will be difficult to evolve naturally or prohibitively slow when the timescales of interest are millions of years. It is also not possible to explore theoretically the behavior of models that have many parameters and/or have been implemented in an explicit, mechanistic manner.

To address this problem, we aim to develop a model of threshold-stochastic fluvial erosion that accounts for realistic, time-varying rainfall, hydrology, and streamflow but retains simplicity, a low number of parameters needing minimal calibration and can handle time steps measured in decades or centuries. To that end, we have integrated a stochastic-mechanistic model of hydrology (Botter et al., 2007, 2009), which has been demonstrated to work well across a range of landscapes and climates (e.g., Basso, Schirmer, & Botter, 2015; Botter et al., 2010; Ceola et al., 2010; Doulatyari et al., 2015; Schaefer et al., 2013) into the threshold-stochastic stream power formulation of Lague et al. (2005). By using a stochastic approach, we can develop analytical solutions that describe the net effect of daily climatic and hydrological processes over long periods, without sacrificing the details of the daily effects. In this way, key thresholds and nonlinearities can be accounted for with a minimum loss of computational efficiency. We establish equations for the daily streamflow distribution and streamflow variability that are applicable across a large range of observed streamflow regimes. The model shows how the distributions of daily streamflow arise from the climatic and hydrological conditions in a river basin. The new climatic and hydrological parameters introduced are rooted firmly in established hydrological theories and many are easily measured from hydrographs and weather station data.

Lague (2014) set out conditions that should be met by any stream power incision model (SPIM) that has been properly temporally upscaled. In developing our model, we stay within the scope of this and previous work on threshold-stochastic (TS)-SPIMs, reproducing results of previous work on the role of the mean and variability in setting the long-term erosion rate (e.g., DiBiase & Whipple, 2011; Lague, 2014; Lague et al., 2005; Tucker & Bras, 2000) and put them in a more general framework by explicitly relating long-term erosion rate to climatic and hydrological conditions. In doing so we aim to better determine which and how hydrological processes influence the relationship between long-term fluvial erosion rates and climate.

## 2. The Hydrological Model

The hydrological model presented in this work is an extension of the physically based stochastic hydrology and soil moisture model laid out in Botter et al. (2007, 2009). In the following sections we summarize key aspects of this model, focusing on those that are relevant to its incorporation into a landscape evolution model.

### 2.1. Rainfall

It is critical that we capture the intermittent and widely variable intensity of daily rainfall. To do this, daily rainfall is modeled after Rodriguez-Iturbe et al. (1999) as a marked Poisson process of rate  $\lambda$ . The subdaily temporal structure of individual storms is not considered. The depths of daily rainfall are considered to be independent and identically distributed random variables,  $p$ , described by an exponential probability density function (pdf)

$$f_p(p) = \frac{1}{\alpha} e^{-p/\alpha}, \quad (1)$$

where  $\alpha$  is the specific mean daily rainfall amount on days with rainfall (i.e., the volume of rainfall divided by the catchment area, referred to as the mean storm depth). We follow this practice for all variables which are measured as volumes integrated over a river catchment. The rate of the Poisson process  $\lambda$  can be interpreted as the mean frequency with which rainfall occurs; thus, we refer to it as the mean storm frequency. The reported range of  $\lambda$  is from  $< 0.05$  to nearly  $1 \text{ day}^{-1}$  and of  $\alpha$  is from 2 to  $> 30 \text{ mm}$  (Deal et al., 2017; Rossi et al., 2016). The specific mean daily rainfall rate is the product of the mean storm depth and the mean storm frequency,  $\bar{p} = \alpha \lambda$  (Rodriguez-Iturbe et al., 1987).

There are some potential issues with using the exponential distribution to represent daily rainfall depths, which we address at the end of the discussion. Regardless, the exponential distribution for daily rainfall depths has been applied with great success in hydrology and ecohydrology, particularly for the characterization of daily soil moisture and streamflow dynamics (e.g., Basso, Schirmer, & Botter, 2015; Botter et al., 2010; Ceola et al., 2010; Doulatyari et al., 2015; Laio et al., 2001; Milly, 1993; Mueller et al., 2014; Park et al., 2014; Porporato et al., 2004; Rodriguez-Iturbe et al., 1999; Settin et al., 2007; Tamea et al., 2010).

### 2.2. Soil Moisture

Soil moisture has come to be recognized as a vital ecological and hydrological feature of river basins, influencing the river response to storm events (e.g., Rodríguez-Iturbe et al., 2006, 2000). The daily soil moisture state

is controlled by its local mass balance, as influenced by rainfall, evapotranspiration, surface runoff and runoff, subsurface flow, and leakage to deeper water reservoirs.

After Botter et al. (2007), we model the effect of these processes on daily streamflow with a physically based model of soil moisture first developed by Rodriguez-Iturbe et al. (1999). For simplicity, we refer to the hydrologically active layer, or the layer of soil that is affected by rainfall and evapotranspiration processes at a daily timescale as the soil layer. The soil layer acts as a reservoir that is filled by random rainfall inputs. Each rainfall event of depth  $p$  replenishes the soil layer which has capacity  $n_{\text{soil}}Z_r$  (where  $n_{\text{soil}}$  is soil porosity with a reported range of 0.35 to 0.55 (Doulatyari et al., 2015; Laio et al., 2001; Porporato et al., 2004) and  $Z_r$  the active or rooting depth with a common value of 500 to 1,000 mm (Doulatyari et al., 2015)) until a critical threshold  $s = s_1$  is reached, after which the soil layer is saturated. At this point, additional rainfall is considered runoff, which recharges the catchment-scale excess water storage and eventually becomes streamflow. In between rainfall events, the soil moisture is reduced by evapotranspiration, which is considered to only occur above the wilting point  $s = s_w$  and increases linearly with increasing soil moisture up to a maximum rate that depends on available energy for vaporization (potential evapotranspiration, PET, reported range of U.S. Geological Survey basins at the annual scale 1.5 to 5.6 mm/d (Rossi et al., 2016)). Since the soil moisture can only range from  $s_w$  to  $s_1$ , the dynamic soil moisture capacity is  $s_o = (s_1 - s_w)n_{\text{soil}}Z_r$ . According to Laio et al. (2001), values for  $s_1$  and  $s_w$  for a variety of soil types range from  $0.35 \leq s_1 \leq 1$  and  $0.11 \leq s_w \leq 0.52$ . For a more in-depth description, see Laio et al. (2001) or Porporato et al. (2004).

This model captures one of the key hydrological processes determining daily streamflow, which is that the soil layer acts as a buffer, capturing and holding incoming rainfall, which allows time for evapotranspiration to return moisture to the atmosphere. The presence of a soil moisture threshold that needs to be exceeded before significant runoff and infiltration processes occur means that the buffer effect is more significant for small storms than large storms. This perspective is put forth in Rossi et al. (2016), where the conclusions are supported by an extensive data set of streamflow mean and variability, as well as basin rainfall and evapotranspiration rates from across the United States. Rossi et al. (2016) demonstrate that the disproportionate effect of the soil layer and evapotranspiration on small and moderate rainstorms has a important impact on the streamflow variability.

In order to know the mean daily streamflow as well as other statistical characteristics of streamflow in a basin, it is necessary to know the mean magnitude and frequency of streamflow generation events, referred to here as floods. Calculating the mean frequency of floods in particular is challenging because the storm depth required to exceed the soil moisture threshold depends on the antecedent soil moisture state, which is time dependent. It has been shown by Porporato et al. (2004) to be  $\omega\lambda$ , where  $\omega$  is a nondimensional filtering factor that is a function of hydrology and climate

$$\omega = \frac{\phi s_*^{\phi} e^{-s_*}}{s_* \Gamma(s_*/\phi) \gamma(s_*/\phi, s_*)}, \quad (2)$$

where  $\Gamma(\cdot)$  is the gamma function,  $\gamma(\cdot, \cdot)$  is the regularized lower incomplete gamma function (see Appendix A for more information on the incomplete gamma functions used in this work),  $\phi$  is the aridity index, and  $s_*$  is the effective soil depth. The effective soil depth describes the capacity of the soil layer to store water relative to the average storm depth,  $s_* = s_o/\alpha$ , and the aridity index is the ratio of the potential evapotranspiration rate to the mean rainfall rate ( $\phi = \text{PET}/\bar{p}$ ). The aridity index has a commonly reported range from nearly 0 to 5 (Gentine et al., 2012; Rossi et al., 2016).

Therefore, the effects of the soil layer (storage and evapotranspiration) on incoming rainfall are captured by  $\omega$ . The soil layer dynamics can have an influence on streamflow generation ranging from very significant ( $\omega = 0.01$ ), where flood frequency and mean daily streamflow are several orders of magnitude less than rainfall frequency and mean, to having almost no effect ( $\omega = 1$ ) (Rossi et al., 2016). The relevant parameters of the soil moisture model are the dynamic soil storage,  $s_o$ , and the maximum evapotranspiration rate, PET, which express the influence of the soil layer conditions on the streamflow ratio. Despite its simplicity and low dimensionality, this minimalist mechanistic-stochastic model has seen wide application and success in predicting probability distributions of catchment-scale daily soil moisture and streamflow (e.g., Doulatyari et al., 2015; Dralle & Thompson, 2016; Feng et al., 2015; Laio et al., 2001; Porporato et al., 2004, 2002; Rodríguez-Iturbe et al., 2006; Settin et al., 2007).

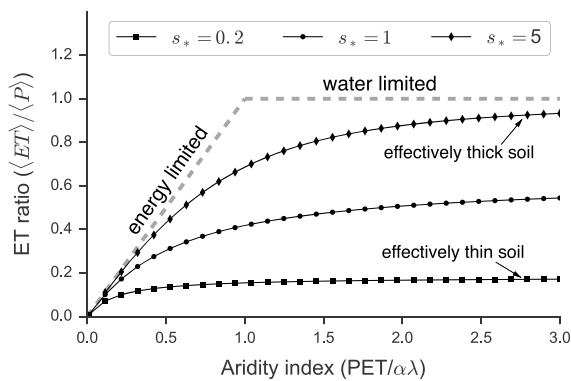


**Figure 1.** Classic energy-limited and water-limited response of evapotranspiration rates to changes in aridity index proposed by Budyko (1974). Expected response of thin- and thick-soiled basins are also shown. Thin-soiled basins never achieve high evapotranspiration rates because a limited amount of water available for evapotranspiration can be stored in the soil water. ET = evapotranspiration; PET = potential ET.

### 2.3. Catchment-Scale Water Balance and the Streamflow Ratio

Here we consider a simplified mean catchment-scale water balance at steady state that can be written as

$$\frac{\langle ET \rangle}{\langle P \rangle} + \frac{\langle Q \rangle}{\langle P \rangle} = 1, \quad (3)$$

where  $\langle P \rangle = \bar{p}A$  is the mean rainfall rate ( $A$  is catchment area),  $\langle ET \rangle$  is the mean loss to evapotranspiration, and  $\langle Q \rangle$  is the mean daily streamflow.  $\langle Q \rangle$  is the product of the mean frequency of floods,  $\omega\lambda$ , and the mean storm depth. Therefore, the fraction of incoming rainfall that is partitioned into streamflow is described by the streamflow ratio  $\omega$

$$\frac{\langle Q \rangle}{\langle P \rangle} = \frac{\alpha\omega\lambda A}{\alpha\lambda A} = \omega, \quad (4)$$

and the specific mean daily streamflow (e.g., mean daily streamflow normalized by catchment area) is simply

$$\mu = \alpha\omega\lambda = \omega\bar{p}. \quad (5)$$

As seen in equation (2), the streamflow ratio is controlled by the effective soil depth,  $s_*$ , and the aridity index,  $\phi$ , two nondimensional numbers that describe the interaction of climate and hydrology. The effective soil depth is a measure of how easily a single storm can saturate the soil layer. When  $s_*$  is small, the average storm can easily saturate the soil, putting the catchment into an effectively thin soil regime. When  $s_*$  is large, the soil is saturated only by intense, rare storms or a rapid sequence of smaller magnitude storms, and the catchment is in an effectively thick soil regime.

The aridity index describes the losses to evapotranspiration relative to the volume of incoming rainfall. It is an established measure of whether a catchment tends toward humid or arid conditions (Budyko, 1974), and is useful for describing a simplified long-term water balance. When  $\phi < 1$ , the rainfall rate exceeds the potential evapotranspiration rate, which leads to energy-limited conditions. In effect, the losses to evapotranspiration are limited by energy available for evapotranspiration rather than water availability, and conditions are humid. When  $\phi > 1$ , conditions are said to be water limited. On average, the capacity for evapotranspiration exceeds the available water, and conditions are more arid (Figure 1).

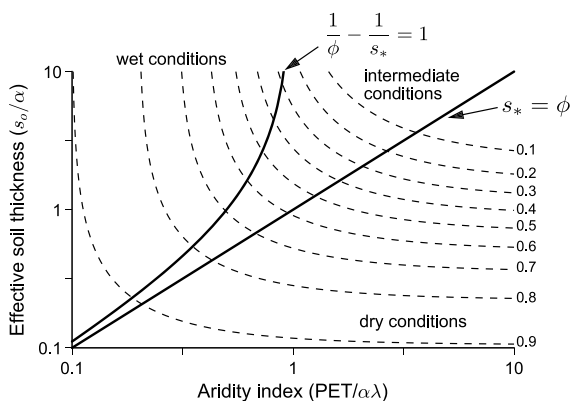


**Figure 2.** The contours denote the value of the streamflow ratio  $\omega$  as a function of the aridity index  $\phi$  and the effective soil capacity  $s_*$  (values shown on righthand side). The wet, intermediate and dry conditions defined by Porporato et al. (2004) are also shown and correspond approximately to humid conditions with effectively thick soil; arid conditions with effectively thick soil; and arid conditions with effectively thin soil, respectively.

The consideration of soil moisture storage capacity,  $s_*$ , further divides humid and arid regimes, leading to four different soil moisture regimes. If  $s_* > 1$  under energy-limited conditions, the catchment is in a humid, thick soil regime and the main control on the streamflow ratio  $\omega$  is the aridity index  $\phi$ . This regime corresponds to the wet regime defined by Porporato et al. (2004) and shown in Figure 2. Although the soil layer is effectively thick, the slow drying rate means that storms will often occur over wet antecedent conditions. This means that even small storms normally incapable of saturating the soil layer may push an already wet soil layer over the threshold and produce a streamflow event. When  $\phi$  and  $s_*$  are both less than one, the catchment is in a humid, thin soil regime and the highest transmission rates of rainfall to streamflow occur. Most storms are able to saturate the soil layer and produce a streamflow event, and the streamflow ratio is not particularly sensitive to either  $\phi$  or  $s_*$ .

When  $s_* > 1$  under water-limited conditions, the catchment is in an arid, thick soil regime,  $\omega$  is small, and the transformation of rainfall to streamflow is dramatically impacted by evapotranspiration. This regime corresponds roughly to intermediate conditions defined by Porporato et al. (2004). The effectively thick and dry soil layer acts as a buffer on incoming storms, absorbing small to moderate storms, and releasing the water from these storms back to the atmosphere through evapotranspiration. Rainfall rates and evapotranspiration potential are balanced, evapotranspiration rates are high, and transmission rates of rainfall to

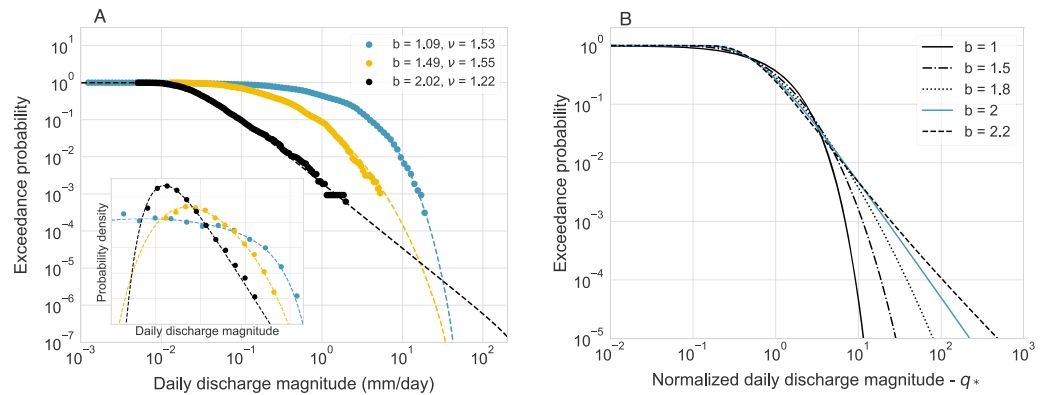


**Figure 3.** (a) The empirical exceedance probability of three U.S. Geological Survey (USGS) stations (colored points) are compared to the best fit  $b$  and  $\nu$  (colored dashed lines). Blue corresponds to summer streamflow (June–August) over the period 1980 to 2014 from USGS station 02298123 (Prairie Creek near Fort Ogden, FL). Yellow corresponds to spring streamflow (March–May) over the period 1980 to 2014 from USGS station 02235200 (Blackwater Creek near Cassia, FL). Black corresponds to summer streamflow (June–August) over the period 1980 to 2014 from USGS station 09430500 (Gila River near Gila, NM). Inset panel shows the same, but as probability densities instead of exceedance probabilities, note both left- and right-hand tails are well fit. (b) Exceedance distributions of streamflow for different recession exponents,  $b$ . All lines correspond to variability index of 1.

streamflow are moderate to low. As a result, both the mean streamflow  $\mu$  and the flood frequency are reduced. The final case is an arid, thin soil regime ( $s_* < 1$ ,  $\phi > 1$ ), corresponding approximately to the dry conditions defined by Porporato et al. (2004) (see Figure 2). Despite high evapotranspiration rates, the role of evapotranspiration is downplayed due to the small soil moisture storage capacity—moderate and even small storms can saturate the soil layer. As a result, effectively thin-soiled basins with high aridity indices will only lose a small to moderate fraction of incoming rainfall to evapotranspiration (Figure 1—effectively thin soil trend).

#### 2.4. Distributions of Daily Streamflow

The hydrological model treats catchments as a simple dynamical system and makes the assumption that storage in the catchment ( $W$ ) is released as river streamflow ( $q$ ) according to a power law relationship ( $q = c_w W^d$ ) (e.g., Kirchner, 2009). This folds much of the hydrological complexity related to how water moves through basins, and how runoff is generated into a few parameters. This is useful here both because we are interested at this point more in the dynamical hydrological response to rainfall than the specific and numerous processes responsible for this response and because such an approach yields a description of streamflow recessions that works well in many places (e.g., Basso, Frascati, et al., 2015; Botter et al., 2009; Kirchner, 2009). This storage-streamflow relationship leads to the time rate change of streamflow being governed by

$$\frac{dq}{dt} = -aq^b + \xi_r, \quad (6)$$

where  $a$  and  $b$  are the recession coefficient and the recession exponent, respectively, and can be related to  $c_w$  and  $d$  (Kirchner, 2009),  $q$  is the (specific) daily streamflow, and  $\xi_r$  is the stochastic effective rainfall forcing. Alternatively, we can write this in terms of a nondimensional streamflow

$$\frac{dq_*}{dt} = -\frac{q_*^b}{\tau} + \frac{\xi_r}{\mu}, \quad (7)$$

where  $q_* = q/\mu$  is daily streamflow normalized by its mean and  $\tau = \mu^{1-b}/a$  is a hydrological response timescale that we discuss in more detail later. Botter et al. (2007) show that the effective rainfall forcing  $\xi_r$  can be well approximated by a Poisson process with the same distribution of depths as rainfall, but a lower rate that is modulated by the streamflow ratio, such that the rate is equal to the flood frequency ( $\omega\lambda$ ).

This leads to three different solutions for the distribution of daily streamflow in terms of hydroclimatic parameters, depending on the value of the recession exponent,  $b$ . For the case  $b = 1$ , Botter et al. (2007) showed that the streamflow distribution is a gamma distribution with shape parameter  $k = \omega\lambda\tau$  and rate parameter  $\beta = \omega\lambda\tau/\mu$ , shown here in nondimensional form

$$f_{Q_*}(q_*) = \frac{(\omega\lambda\tau)^{\omega\lambda\tau}}{\Gamma(\omega\lambda\tau)} q_*^{\omega\lambda\tau-1} \exp[-\omega\lambda\tau q_*]. \quad (8)$$

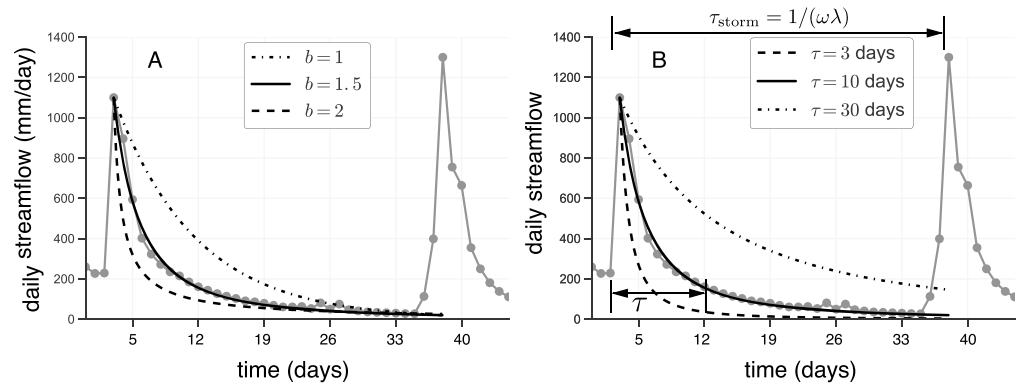


**Figure 4.** An example streamflow recession that has been fit with equation (7) (solid black line,  $b = 1.5$ ,  $\tau = 10$  days). (a) The effect changing recession exponent  $b$  has on the shape of the streamflow recession is shown. (b) Same as in (a) but for changes in response time  $\tau$ .

We present a newly derived distribution of streamflow for the case  $b = 2$  that is an inverse gamma distribution with shape parameter  $k + 1 = \omega\lambda\tau + 1$  and scale parameter  $\beta = \omega\lambda\tau\mu$  (derivation in Appendix B). It is worth noting that this distribution is identical to that from Lague et al. (2005) and  $k$  is the same as that used in Lague et al. (2005), DiBiase and Whipple (2011), Lague (2014), and Scherler et al. (2017)

$$f_{Q_*}(q_*) = \frac{(\omega\lambda\tau)^{\omega\lambda\tau}}{\Gamma(\omega\lambda\tau)} q_*^{-\omega\lambda\tau-2} \exp[-\omega\lambda\tau q_*^{-1}]. \tag{9}$$

This distribution has a power law tail, meaning that it has a much heavier tail relative to the gamma distribution found for  $b = 1$ . The general solution for the case that  $b \neq 1, 2$  is given by Botter et al. (2009) as

$$f_{Q_*}(q_*) = C q_*^{-b} \exp\left[-\omega\lambda\tau \left(\frac{q_*^{2-b}}{2-b} - \frac{q_*^{1-b}}{1-b}\right)\right], \tag{10}$$

where  $C$  is a normalizing constant such that  $\int_0^\infty f_{Q_*}(q_*)dq_* = 1$ . A general analytical solution for  $C$  is challenging, though there are straightforward solutions for certain values of  $b$  as well as analytical approximations (see Appendix C). A particularly useful solution exists for  $b = 1.5$

$$f_{Q_*}(q_*) = \frac{q_*^{-3/2}}{4K_{-1}(4\omega\lambda\tau)} \exp[-2\omega\lambda\tau (q_*^{1/2} + q_*^{-1/2})], \tag{11}$$

where  $K_\nu(\cdot)$  is a modified Bessel function of the second kind. In equation (10) there is an atom of probability,  $p_o$ , that  $q = 0$  for  $0 < b < 1$  (Botter et al., 2009)

$$p_o = C\omega\lambda\tau\mu^{b-1}\delta(q^*). \tag{12}$$

Equation (10) is undefined at  $b = 1, 2$ . However, it can be shown numerically that the limit of equation (10) as it approaches  $b = 1$  is equation (8) and the limit as it approaches  $b = 2$  is equation (9). Further, for  $1 < b < 2$ , equation (10) exhibits probabilities of extreme events between that of the analytical solutions for  $b = 1$  and  $b = 2$  (Figure 3). This allows us to obtain the distribution of streamflow across the observed range of  $b$ . The range of solutions for different values of  $b$  leads to a resolution of the issue of which distribution to use to best represent daily streamflow. Depending on the value of  $b$ , the distribution of streamflow ranges from exponential (light tailed) to power law tailed (heavy tailed). The use of the second parameter  $b$  vastly improves the ability to fit empirical distributions of daily streamflow, which are not all well fit by the inverse gamma distribution (Rossi et al., 2016) (Figure 3). Although flood flashiness  $b$  and the variability index  $\nu$  both influence the variability of daily streamflow, they may express different influences of landscape and climate on streamflow generation.

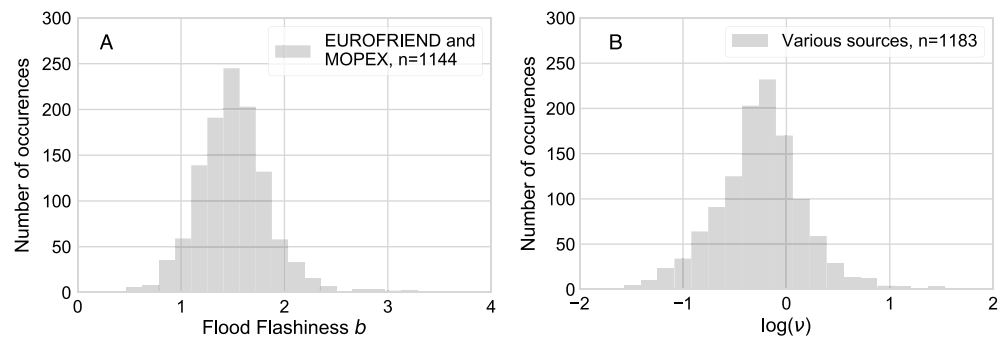


**Figure 5.** (a) The 1,144 observations of recession exponent  $b$ , 725 rivers in Europe (Berghuijs et al., 2016), and 419 in the United States (W. Berghuijs, personal communication, 2017). The values of  $b$  are well distributed around 1.5, with the majority falling between 1 and 2. (b) The 1,183 observations of variability index collected from literature (Lague et al., 2005, Taiwan,  $n = 23$ ; Carretier et al., 2013, West Andes,  $n = 18$ ; Doulatyari et al., 2015, United States,  $n = 44$ ; Basso, Schirmer, & Botter, 2015, United States, Switzerland, and Italy,  $n = 47$ ; Rossi et al., 2016, United States and Puerto Rico,  $n = 653$ ; Scherler et al., 2017, Himalaya and Eastern Tibet,  $n = 398$ ). Variability index shown here represents both annual and seasonal values. The range is larger than discussed previously, from 0.025 to 50, but with most values between 0.1 and 10.

## 2.5. Streamflow Variability

Daily streamflow variability refers how often and by how much the daily streamflow deviates from the mean and can be measured in many ways. In the context of landscape evolution we are concerned in particular with the frequency and magnitude of streamflow events significantly larger than the mean.

The hydrological model used here idealizes hydrographs as being made up of storm impulses followed by streamflow recessions that last until the next impulse. In this idealized case, the variability is controlled by the specifics of streamflow recessions. We model streamflow recessions using equation (7). As a result, streamflow variability is controlled by two factors: the shape of the recessions, determined by the recession exponent  $b$ , and the speed of the recessions relative to the mean time between streamflow generating storms, determined by hydrological response time  $\tau$  and flood frequency  $\omega\lambda$ .

### 2.5.1. The Recession Exponent

The recession exponent  $b$  determines the response of a river basin to a single-storm impulse by dictating the shape of the recession curve (see Figure 4a). When  $b$  is one, the recession follows a decreasing exponential function of time. When  $b$  is greater than one, the response of the basin to an impulse is more dramatic, with a faster drop from the initial high streamflow state to a slower decay at low streamflows. This means that for higher values of  $b$ , the peak of the storm impulse is larger relative to the mean. This leads to a heavier-tailed distribution of daily streamflow, as seen in equations (8)–(10).

While there are some theories as to precisely what determines  $b$  in a river basin (e.g., Biswal & Marani, 2010; Harman et al., 2009; Rupp & Selker, 2006), there is not yet a general consensus (Chen & Krajewski, 2016; Harman et al., 2009). Empirical data sets show that it is likely influenced by climate (Berghuijs et al., 2014), ecohydrology (Szilagyi et al., 2007), land use (Bogaart et al., 2016), and basin geology/geomorphology (Tague & Grant, 2004). For now we consider  $b$  to be an externally defined parameter. Despite uncertainties due to different approaches used for fitting  $b$  (Chen & Krajewski, 2016), empirical distributions from bulk analysis (rather than individual recessions) point to values which mostly fall between 0.5 and 2.5, with values above 3.5 rare (Berghuijs et al., 2016; Bogaart et al., 2016; Ye et al., 2014) (Figure 5a).

The observation that  $b$  is often between one and two implies that distributions of daily streamflow will have tails that are less heavy than power law tails ( $b = 2$ ), but heavier than exponential ( $b = 1$ ). This is well supported by Rossi et al. (2016), which find that the majority of the stations analyzed in the United States have a tail that is lighter than power law, but heavier than exponential.

### 2.5.2. Characteristic Response Time

Two river basins with the same recession exponents can still exhibit fundamentally different recessions. This is because there exists a characteristic timescale for the catchment's hydrological response to a storm

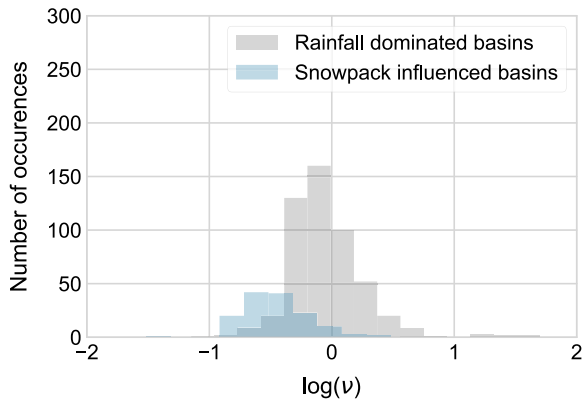


**Figure 6.** Observations of annual variability index from United States and Puerto Rico (Rossi et al., 2016,  $n = 653$ ) divided into catchments with less than 10% annual contribution to water budget by snowfall (rainfall dominated), and those with greater than 10% contribution by snowfall (snowpack influenced). As noted by Rossi et al. (2016), snowpack-influenced catchments have systematically lower variability indices, which agrees with predictions of snowpack accumulation model of Schaeffli et al. (2013).

impulse independent of the shape of the recession set by  $b$  (Figure 4). This timescale captures important catchment-scale hydrological features such as catchment morphology and aspect ratio and average hydrological pathway length and conductivity (Botter et al., 2013). Conceptually, this is similar to defining a half-life for the streamflow recessions.

We can extract the characteristic response time,  $\tau$ , from the recession coefficient  $a$ . Dralle et al. (2015) point out that due to the scaleless nature of the power law describing streamflow recessions, equation (6),  $a$  will exhibit an artificial correlation with  $b$ . They show that there exists a decorrelated recession coefficient  $\hat{a}$  such that  $\hat{a} = aq_o^{b-1}$ , where  $q_o$  is a scaling factor that is basin specific. Here we use the mean daily streamflow  $\mu$  as a proxy for  $q_o$ . Though not perfect, there is some preliminary evidence that this is not a poor choice (Dralle et al., 2015). This defines a new recession coefficient  $\hat{a}$  with units of ( $\text{day}^{-1}$ ). The characteristic timescale for the streamflow recession is then defined as  $\tau = 1/\hat{a}$ .

If the mean time  $\tau_{storm}$  between floods is small compared to the characteristic time  $\tau$  associated with the time for a storm pulse to leave the basin, recessions will sample a narrow range of streamflow magnitudes, and the supply of water to the river will be relatively consistent. This will yield a streamflow regime with low variability. On the other hand if the time it takes for the river basin to drain a storm pulse is small relative to the effective interstorm period, then the recessions will

span a large range of streamflow magnitudes from the highs right after the storm to the lows of baseflow. This will yield a streamflow regime with high variability.

This explains why the shape parameter of the pdf of streamflow from equations (8)–(10) is the ratio of the timescale of the hydrological response to the effective interstorm period. It is known to be a robust description of the streamflow variability in the case  $b = 1$  (Botter et al., 2013). Here we extend it to all values of  $b$  and define it as the variability index. The distribution of  $v$  from variety of climates is shown in Figure 5b.

$$v = \frac{\tau_{storm}}{\tau} = \frac{1}{\omega\lambda\tau} \tag{13}$$

### 2.5.3. Accounting for Snowpack

Schaeffli et al. (2013) develop a simplified method in the same stochastic hydrology framework used here to account for winter streamflow influenced by significant winter snowpack accumulation using three simple assumptions. First, they assume that evapotranspiration does not occur during the winter season. As a result the frequency of floods is equal to the frequency of precipitation because the catchment is not influenced by soil moisture dynamics. Second, they assume that the catchment is divided into two sections. One section that is permanently frozen and does not contribute to streamflow during the winter season, and the rest of the catchment that is still hydrologically active but experiences periodic freezing and accumulation of snowpack. It is assumed that the division of the catchment is a function of its hypsometry and an elevation,  $z^*$ , above which the temperature remains below  $0^\circ\text{C}$  the entire winter season. The final assumption is that the hydrological response time  $\tau$  is increased by the average period of time the mean catchment temperature is below freezing and snowpack is accumulating,  $\tau_D$ , such that the hydrological response time during the winter season is  $\tau_w = \tau + \tau_D$  (Schaeffli et al., 2013). This results in a winter season pdf of daily streamflow when  $b = 1$

$$f_{Q_{w*}}(q_{w*}) = \frac{(\lambda\tau_w)^{\lambda\tau_w}}{\Gamma(\lambda\tau_w)} q_{w*}^{\lambda\tau_w-1} \exp[-\lambda\tau_w q_{w*}], \tag{14}$$

where  $q_{w*} = q/(\mu f_a)$ , and  $f_a$  is the fraction of the catchment active during the winter season. Similarly, in the case that  $b = 2$

$$f_{Q_{w*}}(q_{w*}) = \frac{(\lambda\tau_w)^{\lambda\tau_w}}{\Gamma(\lambda\tau_w)} q_{w*}^{-\lambda\tau_w-2} \exp[-\lambda\tau_w q_{w*}^{-1}]. \tag{15}$$

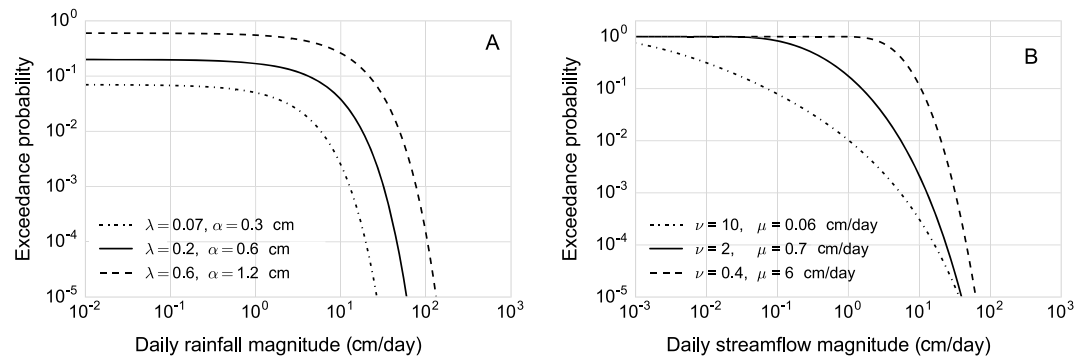


**Figure 7.** Changing the mean rainfall frequency and intensity,  $\lambda$  and  $\alpha$ , while keeping the hydrological conditions constant ( $PET = 5 \text{ mm/d}$ ,  $s_o = 5 \text{ mm}$ ,  $\tau = 5 \text{ days}$ ,  $b = 1.5$ ) demonstrates the covariation of  $\mu$  and  $\nu$ . (a) Three different daily rainfall distributions ranging from high mean rainfall intensity and frequency (dashed line) to low (dash-dotted line). The associated streamflow distributions in (b) range from classically arid (dash-dotted line), with low mean and high variability to classically humid (dashed line), with high mean and low variability.

And for the case that  $b \neq 1, 2$

$$f_{Q_{w*}}(q_{w*}) = C q_{w*}^{-b} \exp \left[ -\lambda \tau_w \left( \frac{q_{w*}^{2-b}}{2-b} - \frac{q_{w*}^{1-b}}{1-b} \right) \right], \quad (16)$$

where  $C$  is again a normalizing constant such that  $\int_0^\infty f_{Q_{w*}}(q_{w*}) dq_{w*} = 1$ .

In river basins where evapotranspiration does not account for a significant fraction of the water balance, the main control on the variability index is the hydrological response time. This conditions is assumed to prevail in basins with significant snowfall during the winter months. Therefore, the proposed model will lead to overall lower variability indices during the winter in these catchments because of the increased response time  $\tau_w$ . This is in broad agreement with Rossi et al. (2016), who find that catchments with  $>10\%$  precipitation as snowfall have systematically lower variability indices (Figure 6).

It must be noted that the variability indices from Rossi et al. (2016) apply to the full year, and the model of Schaeffli et al. (2013) only makes predictions about the winter season. It does not necessarily follow that a low winter variability index must lead to a reduced annual variability index (e.g., when mean streamflow during other seasons is significantly higher or lower than winter mean streamflow, this could lead to an increased annual variability index). Still, the model is shown to perform well in predicting probability distributions of winter streamflow in several alpine catchments (Schaeffli et al., 2013).

Another weakness of this model for winter streamflow is that it does not account for the spike in streamflow associated with springtime melting that must play an important role in determining annual streamflow variability. Finally, much of the uncertainty in the model is hidden by calibrating the elevation parameter  $z^*$  to provide the best fitting pdf rather than determining  $z^*$  a priori. Refer to Schaeffli et al. (2013) for further discussion on the issues inherent in using a minimalistic model to account for winter streamflow in mountainous catchments with snowpack accumulation and melting, which are complex and heterogenous processes.

### 2.6. Daily Streamflow Mean and Variability

Both the daily streamflow mean and variability depend on the flood frequency  $\omega\lambda$ , leading to the following relationship between them

$$\nu = \frac{\alpha}{\tau \mu}. \quad (17)$$

This offers theoretical support for the long-observed negative correlation between  $\mu$  and  $\nu$  (Lague, 2014; Molnar et al., 2006; Rossi et al., 2016), as well as the common observation that dry river basins have high daily streamflow variability. To illustrate this point, Figure 7 shows predicted streamflow probability distributions resulting from a range of mean rainfall intensities and frequencies. As the mean rainfall frequency decreases, the flood frequency decreases which, in turn, causes a decrease in the mean streamflow and an increase in the streamflow variability index. The effect is that the frequency of moderate events is much lower in the dry

basin, while the frequency of large floods is comparable between basins. This is in line with Rossi et al. (2016), who observe a significant difference in the magnitude of frequent streamflow events, but a small difference in the magnitude of rare events between arid and humid basins.

### 3. Integration of Hydrology Into the SPIM

In detachment-limited rivers incising into bedrock, the erosion rate is commonly modeled as a power law of excess shear stress (e.g., Howard, 1994; Tucker & Bras, 2000) of the form

$$\varepsilon = k_e(\tau_s - \tau_c)^{a_t}, \quad \tau_s > \tau_c \quad (18)$$

or of the form (DiBiase & Whipple, 2011; Lague et al., 2005)

$$\varepsilon = k_e(\tau_s^{a_t} - \tau_c^{a_t}), \quad \tau_s > \tau_c, \quad (19)$$

where  $\varepsilon$  is the vertical incision into the riverbed,  $\tau_s$  is the basal shear stress,  $\tau_c$  is the critical shear stress for erosion to occur,  $k_e$  is an erosional efficiency constant, and  $a_t$  an exponent reflecting the dominant erosion process (Whipple et al., 2000). As in Tucker (2004), Lague et al. (2005), and Lague (2014), we use equation (19) because it is more analytically tractable than the original shear stress incision model proposed by Howard et al. (1994) and Tucker and Bras (2000). In order to relate streamflow to shear stress, it is necessary to know the channel cross-sectional profile and roughness. To obtain this, we make common assumptions about channel width and depth as a function of mean streamflow and daily streamflow (e.g., DiBiase & Whipple, 2011; Lague, 2014; Lague et al., 2005). This results in the following expression for the daily incision as a function of daily streamflow, mean daily streamflow, and channel slope (Lague et al., 2005)

$$\varepsilon = K \langle Q \rangle^{m_c} S^{n_c} q_*^\gamma - \psi, \quad q > q_c. \quad (20)$$

$$K = k_e k_t^{a_t} k_w^{-a_t a_t}; \quad m_c = a_t \alpha_t (1 - \omega_b); \quad n_c = a_t \beta_t; \quad \gamma = a_t \alpha_t (1 - \omega_s); \quad \psi = k_e \tau_c^{a_t}. \quad (21)$$

For more information on channel hydraulic parameters ( $\alpha_t$ ,  $\beta_t$ ,  $k_t$ ,  $k_w$ ,  $\omega_b$ , and  $\omega_s$ ) and the derivation in general see Appendix D.  $K$  is an erodibility coefficient that is a function of channel hydraulics and lithology but not climate,  $q_* = q/\mu$  is the normalized specific daily streamflow,  $\langle Q \rangle$  is the mean daily catchment integrated streamflow ( $\langle Q \rangle = \mu A$ ),  $S$  is the river slope, and  $\psi$  is the threshold for erosion. The exponents  $m_c$ ,  $n_c$ , and  $\gamma$  are determined by the channel form and hydraulics, as well as dominant erosion process. The exponent  $n_c$  determines the relative importance of the river slope. The exponent  $m_c$  is related to the downstream scaling of channel width. In contrast, the exponent  $\gamma$  describes the at-a-station channel width with the daily variations in streamflow and therefore controls the sensitivity of the daily erosion rate to streamflow variability. When  $\gamma > 1$  shear stress  $\tau_s$  increases disproportionately to daily streamflow, and large floods will be more important in determining the long-term erosion rate than when  $\gamma \leq 1$ .

Equation (20) is the instantaneous incision rate due to the streamflow magnitude  $q$ . Our goal is to use knowledge of the probability distribution of  $q$  to temporally upscale (20) into a SPIM of the form

$$\langle E \rangle = K' k_s^n = K' A^m S^n, \quad (22)$$

where  $k_s = SA^{\frac{m_c}{n_c}}$ .  $K'$  may be a function of channel hydraulics, erosion thresholds, climate, hydrology, and anything else deemed important, but it is independent of both catchment area  $A$  and channel slope  $S$ .

To obtain the upscaled SPIM, previous studies integrated the magnitude of daily incision as a function of streamflow, weighted by the probability of observing a particular streamflow magnitude (e.g., DiBiase & Whipple, 2011; Huang & Niemann, 2006b; Lague, 2014; Lague et al., 2005; Tucker & Bras, 2000)

$$\langle E \rangle = \int_{q_c}^{q_{m^*}} \varepsilon(q_*) f_{Q_*}(q_*) dq_*, \quad (23)$$

where  $\langle E \rangle$  is the mean long-term erosion rate, the lower bound of the integral is the critical streamflow that exceeds the erosion threshold, and the upper bound is the maximum streamflow expected in the period of observation. Conceptually, there is a small problem with this approach which may matter when the maximum

streamflow is relatively low ( $q_m < 100\mu$ ) or when the variability is high (see Appendix E for details). To properly account for a maximum streamflow, the pdf of streamflow should be truncated at  $q = q_m$  and renormalized, producing a new pdf  $f_Q^t(q | q_m)$  that has zero probability of  $q > q_m$ , and can be safely integrated to infinity, leading to

$$\langle E \rangle = \int_{q_{c*}}^{\infty} \varepsilon(q_*) f_{Q_*}^t(q_* | q_{m*}) dq_* = \frac{\int_{q_{c*}}^{q_{m*}} \varepsilon(q_*) f_{Q_*}(q_*) dq_*}{\int_0^{q_{m*}} f_{Q_*}(q_*) dq_*} \quad (24)$$

Though this approach is effective, in the final derivation, we use a different approach that is functionally equivalent, but we feel provides a firm theoretical basis for future work (see Appendix E for derivation).

The upscaled SPIM is

$$\langle E \rangle = \mu_\varepsilon K \mu^{m_\varepsilon} A^{m_\varepsilon} S^{n_\varepsilon} - \lambda_\varepsilon \psi, \quad (25)$$

where

$$\mu_\varepsilon = \int_{q_{c*}}^{\infty} q_*^\gamma f_{Q_*}^t(q_* | q_{m*}) dq_* = \frac{\int_{q_{c*}}^{q_{m*}} q_*^\gamma f_{Q_*}(q_*) dq_*}{\int_0^{q_{m*}} f_{Q_*}(q_*) dq_*} \quad (26)$$

is the nonlinear average of daily streamflow above the threshold. This is similar to the most effective streamflow defined in the classic work of Wolman & Miller (1960, their Figure 1). The second new variable

$$\lambda_\varepsilon = \int_{q_{c*}}^{\infty} f_{Q_*}^t(q_* | q_{m*}) dq_* = \frac{\int_{q_{c*}}^{q_{m*}} f_{Q_*}(q_*) dq_*}{\int_0^{q_{m*}} f_{Q_*}(q_*) dq_*} \quad (27)$$

is the probability of streamflow exceeding the threshold, which can be thought of as an erosion frequency akin to the rainfall frequency  $\lambda$ . Both  $\mu_\varepsilon$  and  $\lambda_\varepsilon$  have analytical solutions for the case of  $b = 1, 2$  (see Appendix G).

A useful and common approximation to make is to assume the maximum streamflow is so large that it can be treated as infinite (DiBiase et al., 2010; Lague, 2014; Snyder et al., 2003; Tucker, 2004; Tucker & Bras, 2000). Then the truncated pdf in equations (26) and (27) can be replaced with the original pdf of streamflow,  $f_{Q_*}(q_*)$ , leading to simpler analytical forms of  $\mu_\varepsilon$  and  $\lambda_\varepsilon$ . This approximation is helpful in simplifying the math and is generally safe to make (Lague et al., 2005). However, it is possible, particularly for heavier-tailed distributions with high variability indices, that assuming much larger maximum streamflows than are actually observed could lead to overpredicted erosion rates. With the approximation  $q_{m*} \sim \infty$ ,  $\mu_\varepsilon$  and  $\lambda_\varepsilon$  are

$$\mu_\varepsilon = \begin{cases} \frac{\Gamma(1/\nu + \gamma)}{\Gamma(1/\nu)^{\nu - \gamma}} \Gamma(1/\nu + \gamma, q_{c*}/\nu); & b = 1 \\ \frac{K_{(2\gamma-1)}(4/\nu)}{\Gamma(2\gamma-1)} \Gamma_g(2\gamma-1, 2\sqrt{q_{c*}}/\nu; 4/\nu^2); & b = 1.5 \\ \frac{K_{-1}(4/\nu)}{\Gamma(1/\nu)^{\nu-1}} \gamma(1/\nu + 1 - \gamma, 1/\nu q_{c*}); & b = 2 \end{cases} \quad (28)$$

$$\lambda_\varepsilon = \begin{cases} \Gamma(1/\nu, q_{c*}/\nu); & b = 1 \\ \Gamma_g(-1, 2\sqrt{q_{c*}}/\nu; 4/\nu^2); & b = 1.5 \\ \gamma(1/\nu + 1, 1/\nu q_{c*}); & b = 2 \end{cases} \quad (29)$$

where  $\Gamma(\cdot)$  is the upper regularized incomplete gamma function,  $\gamma(\cdot)$  is the lower regularized incomplete gamma function, and  $\Gamma_g(\cdot, \cdot)$  is the generalized upper regularized incomplete gamma function (see Appendix A for details on the special functions used here). This last function is not as useful as the other special functions used here because it is not included in standard computational packages. However, there do exist algorithms to calculate  $\Gamma_g(\cdot, \cdot)$  that should be computationally cheaper than direct numerical integration of (26) and (27) (Chaudhry et al., 1996; Veling, 2011). For the case  $b \neq 1, 1.5, \text{ or } 2$ , equations (26) and (27) can be integrated numerically. We see from (28) and (29) that the influence of hydrology on the upscaled SPIM is expressed entirely by  $\nu$ ,  $b$ , and  $\mu$ .

Although equation (25) is an upscaled SPIM, it is not in the desired form of equation (22), because the proper scaling between  $\langle E \rangle$  and  $k_\varepsilon$  is not clear due to the dependence of the critical streamflow  $q_{c*}$  on channel slope  $S$ . In section 3.1 we discuss further how the scaling can be extracted from this SPIM.

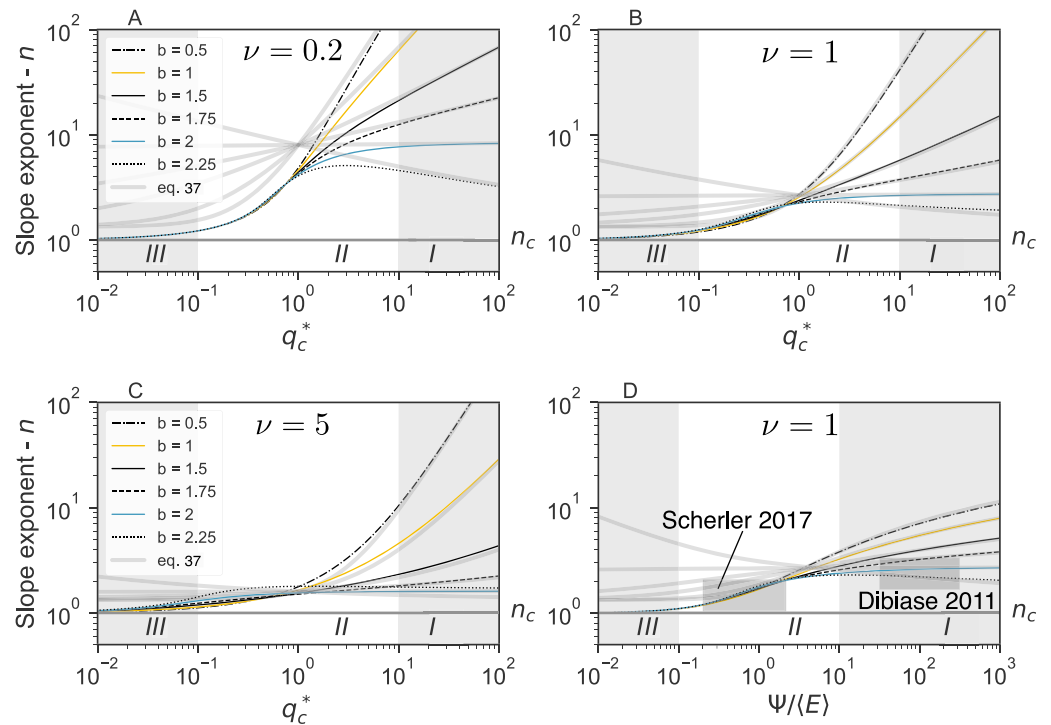


**Figure 8.** Slope exponent,  $n$ , as a function of  $q_{c^*}$  and  $b$  computed using equation (25) (blue, black, and gold lines) compared to the approximation of  $n_s$  from equation (37) (light gray lines). (a) shows  $\nu = 0.2$ , (b) shows  $\nu = 1$ , and (c) shows  $\nu = 5$ . We also set  $\gamma = 0.75$  for (a)–(d), which is argued to be the most common value (DiBiase & Whipple, 2011). The three regimes discussed in text are labeled in all panels. (d)  $n$  as a function of the erosion threshold normalized by mean long-term erosion rate instead of mean daily streamflow. While  $n$  is larger when  $b < 2$  compared to  $b = 2$ , the slope exponent takes on reasonable values within the observed range of normalized erosion thresholds. For reference, the gray boxes correspond to conditions in the Himalaya and Eastern Tibet (Scherler et al., 2017, assuming variable  $D_{50}$  and  $\tau_c$  and  $100 \leq k_{s,n} \leq 400$ ), as well as the San Gabriel Mountains (DiBiase & Whipple, 2011), though the variability index is not 1 for all rivers in these locations.

### 3.1. Controls on TS-SPIM Slope Exponent

Lague (2014) defined two classes of upscaled SPIMs: those that take into account erosion thresholds and streamflow variability, referred to as TS-SPIMs, and those that use a constant effective streamflow with no thresholds, referred to as constant-discharge SPIMs (CD-SPIMs). Further, there are three established regimes that rivers can exist in for which the parameters  $K'$  and  $n$  are defined differently. These regimes depend on the magnitude of the erosion threshold (DiBiase & Whipple, 2011; Lague et al., 2005). When the erosion threshold is small ( $q_{c^*} \ll 1$ ), the CD-SPIM is accurate (DiBiase & Whipple, 2011; Lague et al., 2005), and the river is in regime III (Figure 8). In this case, it can be shown that the SPIM derived here (25) collapses to a CD-SPIM in the form we seek

$$\langle E \rangle = K_{cd} k_s^{n_c} = K_{cd} A^{m_c} S^{n_c} \quad (30)$$

$$K_{cd} = \mu_\epsilon K \mu^{m_c} \quad (31)$$

assuming  $q_{c^*} = 0$  and  $q_{m^*} \sim \infty$ , where

$$\mu_\epsilon = \begin{cases} \frac{\Gamma(1/\nu + \gamma)}{\Gamma(1/\nu)\nu^{-\gamma}}; & b = 1 \\ \frac{K_{(2\gamma-1)}(4/\nu)}{K_{-1}(4/\nu)}; & b = 1.5 \\ \frac{K_{-1}(4/\nu)}{\Gamma(1/\nu + 1 - \gamma)}; & b = 2 \end{cases} \quad (32)$$

In this case,  $K_{cd}$  is independent of channel slope and catchment area, and  $n_c$  captures the scaling of the steepness index with erosion rate.

DiBiase and Whipple (2011) defined regime I for rivers with large erosion thresholds ( $q_{c*} \gg 1$ ). In this regime, the TS-SPIM applies and the CD-SPIM is inaccurate. Specifically, in the case of  $b = 2$ , Lague (2014) provides an equation for TS-SPIM in the form of (25)

$$\langle E \rangle = K_{ts} k_s^{n_s} = K_{ts} A^{m_s} S^{n_s} \quad (33)$$

$$K_{ts} = \left( \frac{\gamma \Gamma(1/\nu + 2)^{-1}}{(1 + \nu - \gamma \nu) \nu^{1/\nu}} \right) \psi^{1 - \frac{n_s}{n_c}} K^{\frac{n_s}{n_c}} \mu^{m_s} \quad (34)$$

$$n_s = \frac{n_c}{\gamma} \left( \frac{1}{\nu} + 1 \right) = \frac{\beta_t (1 + \omega \lambda \tau)}{\alpha_t (1 - \omega_s)} \quad (35)$$

$$m_s = \frac{m_c}{n_c} n_s = \frac{m_c}{\gamma} \left( \frac{1}{\nu} + 1 \right). \quad (36)$$

In general, the equation for  $K_{ts}$  is not yet known in this regime. However, using the symmetry between equations (8)–(10), we propose an approximation for the channel slope exponent when  $q_{c*} \gg 1$ , valid for  $0 < b < 2.5$

$$n_s = \frac{n_c}{\gamma} \left( \frac{q_{c*}^{2-b}}{\nu} + 1 \right) = \frac{\beta_t (1 + \omega \lambda \tau q_{c*}^{2-b})}{\alpha_t (1 - \omega_s)}. \quad (37)$$

The accuracy of this equation is demonstrated in Figure 8. Similarly, it can be shown that the area exponent in regime I can be approximated as

$$m_s = \frac{m_c}{\gamma} \left( \frac{q_{c*}^{2-b}}{\nu} + 1 \right) = \frac{1 - \omega_b}{1 - \omega_s} (1 + \omega \lambda \tau q_{c*}^{2-b}). \quad (38)$$

Therefore, the SPIM predicts that profile concavity  $\theta = \frac{m}{n}$  should not change as a function of threshold-stochastic effects because  $\frac{m_s}{n_s} = \frac{m_c}{n_c}$ . In between regime I and III is the transition regime, II, which occurs when  $q_{c*}$  is in the neighborhood of 1. Here  $K'$  and  $n$  take on transitional values between those of the TS-SPIM and the CD-SPIM (Figure 8).

The observation that the exponent on channel slope is often significantly larger than 1 when the SPIM is fit to river profiles (DiBiase et al., 2010; Ouimet et al., 2009; Snyder et al., 2003) is problematic for the CD-SPIM, whose slope exponent,  $n_c$ , is a function of the dominant erosion mechanism and channel cross-sectional profile and should be close to 1 and not larger than 2 for most proposed models (Lague, 2014; Lague et al., 2005). In contrast, the slope exponent of the TS-SPIM,  $n_s$ , is also a function of climate, not just channel hydraulics, and will be systematically larger than  $n_c$  (Lague, 2014), which compares more favorably with observed slope exponents.

The TS slope exponent computed using equation (37) is compared to the slope exponent  $n$  computed from the full SPIM (equation (25)). When  $b < 2$ , the slope exponent becomes a function of the erosion threshold, increasing the degree of nonlinearity of channel slope compared to when  $b = 2$ . The flood flashiness,  $b$ , is often observed to be less than 2 (Berghuijs et al., 2014; Rossi et al., 2016). The resulting dependence of the TS slope exponent on  $q_{c*}$  means that it is sensitive to controls on  $q_{c*}$ , in particular the specific mean streamflow and the grain size distribution in the river. It also means that channel slope is likely to have an influence on its exponent through the critical streamflow.

The TS-SPIM provides an explanation for observed slope exponents significantly larger than one; however, the slope exponents it predicts may actually be too large. Lague (2014) makes the observation that many mountainous rivers are firmly in regime I (albeit with the assumption  $b = 2$ ), which implies large slope exponents, particularly when the variability index is small (Figure 8). This is at odds with the fact that slope exponents have rarely been observed larger than 4 (DiBiase et al., 2010; Ouimet et al., 2009; Scherler et al., 2014). To some extent, this mismatch is tempered by the fact that erosion is very slow in low variability, high threshold regimes that should have very high slope exponents (i.e., if such rivers exist, they are not the ones whose slope exponents are measured). Figure 8d shows the slope exponent where the erosion threshold is normalized by mean long-term erosion rate instead of mean streamflow. The slope exponent takes on more reasonable

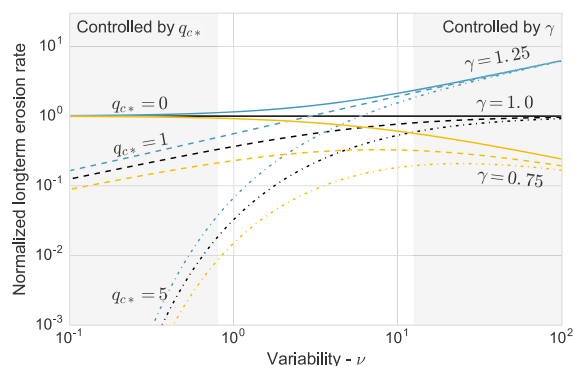


**Figure 9.** At low streamflow variability the erosion threshold  $q_{c*}$  controls the erosion efficiency, with the erosion rate decreasing progressively as the erosion threshold is increased from 0 (solid lines) to 1 (dashed lines) to 5 (dashed-dotted lines). At high streamflow variability, the erosion nonlinearity  $\gamma$  becomes the dominant control, and the erosion efficiency increases as  $\gamma$  increases from 0.75 (yellow lines) to 1 (black lines) to 1.25 (blue lines). Here  $b = 1.5$ , but the trends are qualitatively similar for  $1 \leq b \leq 2.5$ .

values within the observed range of normalized erosion thresholds. Regardless, Figure 8 illustrates that the TS-SPIM exhibits a wider range in the slope exponent than observed. The lack of slope exponents larger than 4 still merits further study. The mismatch could imply that hydrology and hydraulics do not play as important a role as expected.

One encouraging result is found in Scherler et al. (2017), who investigate slope exponents in the Himalaya and Eastern Tibet. They find exceptionally low variability indices; however, the mean streamflow is very high, leading to  $q_{c*} \leq 1$ , with the implication that these rivers are mostly in regimes II and III. The slope exponents they find, between 1 and 2, are in the correct range. And indeed, the erosion rates are best collapsed by a SPIM with small erosion thresholds.

### 3.2. Daily Streamflow Variability and Long-Term Erosion Rate

According to equation (25), the long-term erosion efficiency varies as a function of streamflow variability index (Figure 9). Erosion efficiency is measured by the normalized long-term erosion rate, defined as the long-term erosion rate  $\langle E \rangle$  divided by the constant streamflow reference erosion rate  $\epsilon_o = K\langle Q \rangle^{m_c} S^{n_c}$  (arrived at when there are no threshold effects and when  $\gamma = 1$ ). This highlights the influence of the variability of daily streamflow and the erosion threshold.

In general, when the variability index is large, erosion efficiency is controlled by the at-a-station nonlinearity,  $\gamma$  (see Figure 9). Erosion efficiency increases with increasing variability when  $\gamma > 1$  because of the strengthened influence of large floods and decreases with increasing variability when  $\gamma < 1$  because of the weakened influence of large floods. In contrast, when the variability index is small, erosion efficiency is controlled by the erosion threshold  $q_{c*}$ . When the variability index is small, erosion efficiency decreases with increasingly higher thresholds, regardless of the value of  $\gamma$ . These results are consistent for  $1 \leq b \leq 2.5$  and are in line with previous work (Lague et al., 2005; Tucker & Bras, 2000). This suggests that for a wide range of conditions, the erosion threshold will be a dominant factor in setting the long-term erosion rate for  $\nu \leq 1$ .

#### 3.2.1. The Role of $b$

Larger values of  $b$  lead to heavier-tailed distributions of daily streamflow. Rare streamflow events associated with heavier-tailed distributions are larger than equally rare events from light-tailed distributions. Thus, the effect of increasing  $b$  is similar to increasing the variability index,  $\nu$ . Higher  $b$  values also lead to increased sensitivity to  $\gamma$  when the variability index is large and a lowered sensitivity to the erosion threshold when the variability index is small. Hydrological and geomorphological conditions are often implicated as controls on  $b$  (Bogaart et al., 2016; Szilagyi et al., 2007; Tague & Grant, 2004). In this way, they can influence the efficiency of fluvial erosion for different dominant processes, channel cross sections (setting  $\gamma$ ), and erosion thresholds.

The magnitude of the effect that changes in the variability index have on the erosion rate will differ for different values of  $b$ . One consequence of this is that if  $b$  and  $\nu$  covary, the response to increasing variability will be compounded by increasing  $b$  and will be more significant than would be predicted for a constant  $b$  value.

#### 3.2.2. The Importance of Maximum Streamflow for Power Law-Tailed Streamflow Distributions

For heavy-tailed distributions ( $b \geq 2$ ), the long-term mean erosion rate does not necessarily converge to a constant value, even for long observation periods. Instead, the measured long-term erosion rate may fluctuate continuously over time. However, if there exists a physical upper limit on the magnitude of daily streamflow  $q_{m*}$ , the erosion rate will converge to a mean value once the observation period is long enough to have a good probability of including  $q_{m*}$ . Thus, the existence of maximum streamflow has a significant impact on the existence of a long-term mean erosion rate, especially when  $b \geq 2$  and  $\gamma \geq 1$ . Despite the critical role of the maximum streamflow, the precise value of  $q_{m*}$  is often not important in determining the long-term mean erosion rate, it is only important that it exist. This was also noted by Lague et al. (2005) who showed that the value of  $q_{m*}$  is only important in limited regimes ( $b \geq 2$ ,  $\nu > 1$  and  $\gamma > 1$ ).

## 4. Discussion

The hydrological model creates a framework where only the daily mean and variability of streamflow ( $\mu$  and  $\nu$ ) and the recession exponent  $b$  are needed to fully specify the distribution of daily streamflow and to relate that distribution back to the climatic and hydrological conditions giving rise to it. This allows us to bring hydrology

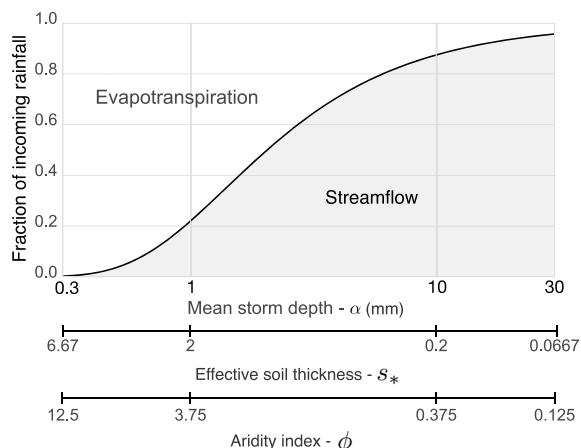


**Figure 10.** The interaction of climatic and hydrological conditions (expressed as  $s_*$  and  $\phi$ ) is what determines the water partitioning in a catchment. The hydrological conditions are held constant ( $PET = 0.5 \text{ cm/d}$ ,  $\lambda = 0.4$ , soil capacity  $n_{\text{sol}}Z_r(s_1 - s_w) = 2 \text{ cm}$ ) while the mean storm intensity is varied ( $0.2 \text{ cm} < \alpha < 20 \text{ cm}$ ). The result is that the relative importance of hydrological processes such as soil moisture storage and evapotranspiration changes across the range of storm depths, with the fraction of rainfall lost to evapotranspiration and interception decreasing significantly with increasing storm depth.

into an upscaled SPIM and unite the work of Tucker and Bras (2000) with the work of Crave and Davy (2001) and Lague et al. (2005). These workers established two different theoretical bases of stochastic climatic forcing in landscape evolution that have been used in several subsequent studies (Carretier et al., 2013; Collins et al., 2004; DiBiase & Whipple, 2011; Istanbuloglu & Bras, 2005, 2006; Lague, 2014; Molnar et al., 2006; Rossi et al., 2016; Scherler et al., 2017; Snyder et al., 2003; Tucker & Bras, 2000). Tucker and Bras (2000) and Tucker (2004) consider the effect of realistic stochastic climate forcing but neglect hydrology, arriving at a light-tailed exponential distribution for streamflow and representing the variability of climate with a parameter that can be described as one over the storm frequency  $1/\lambda$ . In contrast, Lague et al. (2005) consider hydrology directly, using a heavy-tailed distribution for streamflow commonly observed in nature and representing climatic variability with the shape parameter of their heavy-tailed distribution  $k$ . However, this is done at the expense of the connection to realistic climatic forcing, as the distribution of streamflow cannot be cast in terms of rainfall. Within the framework presented here, a light-tailed distribution of streamflow and a solution for the long-term erosion rate very similar to Tucker & Bras, (2000, their equation (33)) is recovered when  $b = 1$ . When  $b = 2$ , the streamflow distribution is heavy tailed, and the solution for the long-term erosion rate is equivalent to Lague et al. (2005, their equation (17) (assuming  $q_{m*} \sim \infty$ )). Furthermore, the different concepts of climatic variability can be reconciled in this framework with the variability parameter  $\nu = 1/k = (\omega\lambda\tau)^{-1}$ , which is equivalent to one over Lague's variability  $k$ , and a linear function of Tucker's variability  $1/\lambda$ .

The hydrological model allows us to understand how the mean and variability of streamflow respond to changes in the climatic and hydrological boundary conditions. In turn, the influence that streamflow mean and variability have on stream power erosion has been clearly investigated in previous studies (e.g., Lague, 2014; Lague et al., 2005) and is well understood. As a result, the streamflow variability index  $\nu$  and the mean streamflow  $\mu$  provide a useful way to understand the effect of hydrology and climate on long-term fluvial erosion rates.

#### 4.1. Hydrologic and Climatic Controls on Streamflow

Neither the climate nor the hydrology of a river basin alone dictates the resulting streamflow distribution, but rather the interaction between the two. This means that the same climate can give rise to different fluvial responses depending on the hydrological regime, leading to the conclusion that the erosional response to a given climate cannot be predicted without taking into account the hydrology of a river basin.

However, the manner in which the soil layer dynamics and evapotranspiration modulate climate to yield the streamflow regime (described by  $\mu$ ,  $\nu$ , and  $b$ ) is not straightforward. These processes effect both the total amount of water transmitted through the hydrological system to the river as well as the frequency of floods and consequently the streamflow variability. In some cases they act as a strong filter, fundamentally altering the statistics of incoming rainfall. In other cases these processes are less important, leaving the statistics of rainfall relatively intact as they are transmitted through the basin to become the statistics of streamflow.

##### 4.1.1. Mean Streamflow

One of the most important influences the hydrological conditions in a river basin have on the mean streamflow is to control the fraction of the incoming rainfall enters the fluvial system (expressed by the streamflow ratio  $\omega$ ). The reduction of the mean streamflow relative to incoming rainfall can be significant, with arid catchments approaching 100% loss of incoming rainfall to evapotranspiration (Budyko, 1974; Lehner et al., 2017; Thompson et al., 2011).

Two basins with similar mean rainfall rates, but different soil depths or evapotranspiration rates can have significant differences in the mean streamflow rates. When the mean storm size is large compared to the soil capacity, the soil layer is easily saturated, and most storms produce runoff events. In this case the streamflow ratio is close to one, and the intensity and frequency of streamflow events are closely correlated with the mean and frequency of rainfall. As the storm size decreases relative to soil storage capacity,

the effective soil depth increases, and the soil layer is saturated only by increasingly infrequent, large storms. This results in fewer runoff events, as larger fractions of each storm are stored in as soil moisture, and eventually lost to evapotranspiration. It also results in a larger aridity index, and reduced mean streamflow (Figure 10). This leads to the conclusion that mean streamflow may be significantly influenced by factors other than the mean rainfall rate in a river basin, including temperature, insolation, slope aspect, soil depth and porosity, and vegetation type and cover. These factors can change over time, thereby influencing the long-term evolution of a river basin.

The partitioning of rainfall into streamflow and evapotranspiration can also respond nonlinearly to changes in rainfall intensity or frequency, such that changes in mean rainfall rate have a disproportionate effect on mean streamflow (Figure 10). Additionally, mean streamflow may respond differently to a change in mean rainfall intensity than it does to a change in mean rainfall frequency, even if the change to mean rainfall rate is the same in both cases. This is because the rainfall intensity and frequency have different influences on the effective soil thickness and aridity index.

All else constant, catchments in the thick and/or dry soil regimes will require steeper riverbed slopes to achieve the same erosion rate compared to catchments with effectively thinner, wetter soils but with the same mean rainfall rate because the associated mean streamflow rate will be lower. To the extent that vegetation is correlated with thicker soils and higher evapotranspiration rates (leading to the dry thick soil regime), extensively vegetated catchments could experience slower erosion for the same steepness not only because of the vegetation's ability to stabilize slopes but also because of its role in reducing the erosiveness of the rivers by a (potentially significant) reduction in the mean daily streamflow relative to the incoming mean rainfall (Lehner et al., 2017; Thompson et al., 2011). Similarly, arid catchments are expected to use each millimeter of rainfall less efficiently for erosion due to more significant losses to atmospheric fluxes. However, this may be obfuscated by other differences such as the erosion threshold or streamflow variability that are also expected to vary systematically between catchments in different hydrological regimes.

#### 4.1.2. Streamflow Variability

The retention of rainfall in the soil layer, and its release back into the atmosphere via evapotranspiration does not only reduce the mean streamflow but also causes a shift in the statistics of runoff events relative to rainfall. This is well supported by the study of the environmental controls on streamflow variability in several hundred river basins in the United States and Puerto Rico (Rossi et al., 2016). This study finds that the increase in streamflow variability associated with increasing basin aridity can be understood as a decrease in the frequency of moderate streamflow events (event return period 0.2–2 years) relative to rare streamflow events (event return period > 20 years). Rossi et al. (2016) attribute this to the increased likelihood in arid basins for small and moderate rainfall events to be captured in the soil layer of the basin, and subsequently lost to evapotranspiration. The study additionally finds that the basin aridity index,  $\phi$ , evapotranspiration ratio,  $ET_{rat}$ , and the rainfall frequency,  $\lambda$ , are the best predictors of streamflow variability in rainfall dominated catchments (<10% precipitation as snow). Finally, Rossi et al. (2016) observe that mean and variability of daily rainfall intensity are poor predictors of streamflow variability, suggesting that these are not important controls.

These findings match well with the environmental controls on the streamflow variability index described by our model as well as the conceptual description of how effectively thin or thick, wet or dry soil regimes drive the streamflow ratio, and consequently the streamflow variability index. Equation (13) predicts that the variability index is controlled by hydrological response time, mean rainfall frequency, and the runoff ratio, itself a function of the effective soil thickness and the aridity index ( $v = [\omega(s_*, \phi)\lambda\tau]^{-1}$ ). Rossi et al. (2016) do not assess the relationship between soil moisture storage capacity or hydrological response time and streamflow variability, but the relationships found between aridity index and streamflow variability as well as mean rainfall frequency and streamflow variability are well captured by our model.

To show this, we use Monte Carlo techniques to probe the controls on streamflow variability predicted by the model over a wide range of climatic and hydrological conditions (Figure 11). Under energy-limited conditions ( $\phi < 1$ ), the variability is mostly controlled by the hydrological response time. When conditions are water limited ( $\phi > 1$ ), streamflow variability is predominantly controlled by the effective soil depth,  $s_*$ . The control of the effective soil depth reflects both the importance of soil moisture storage capacity and mean rainfall intensity. However, we note that Rossi et al. (2016) find mean rainfall intensity to be a poor predictor of streamflow variability, which may imply that the model overemphasizes the role of the effective soil depth.

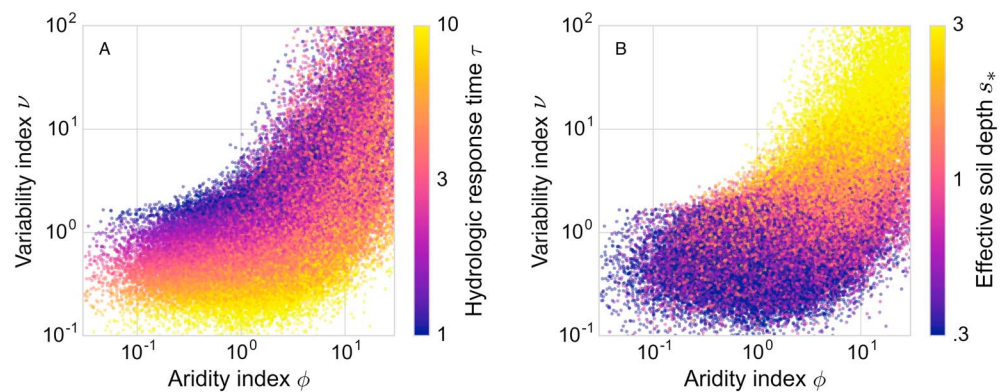


**Figure 11.** Monte Carlo simulations of the streamflow variability index for a wide range of hydrological and climatic boundary conditions ( $PET = 0.2\text{--}20\text{ mm/d}$ ,  $\alpha = 0.25\text{--}25\text{ mm}$ ,  $\lambda = 0.01\text{--}1\text{ day}^{-1}$ ,  $s_o = 0.5\text{--}10\text{ mm}$ ,  $\tau = 1\text{--}10\text{ days}$ ). The parameters are chosen randomly from either uniform distributions or uniform distributions in logarithmic space. (a) For a wide range of conditions, hydrological response time is an important control on variability in humid basins ( $\phi < 1$ ). (b) Effective soil depth is also an important control on variability, but for arid basins rather than humid ones ( $\phi > 1$ ). Finally, the aridity index is an important overall control on variability, with humid basins tending to be less variable than wet basins.

Finally, across a wide range of climatic and hydrological conditions, streamflow variability is predicted to be higher under more arid conditions (Figure 11). This matches the observation from Rossi et al. (2016) and others that the variability of daily streamflow increases in more arid conditions (e.g., DiBiase & Whipple, 2011; Molnar et al., 2006).

#### 4.1.3. Hydrology, Climate, and Erosion

It is useful to understand independently the influence of streamflow mean and variability (variability index and flashiness) on the long-term erosion rate as we have done above. However, the relationship between streamflow mean and variability index that emerges from the theory presented in this study (equation (17)) suggests that the two should be considered together. This is supported by widespread observations of a negative correlation between streamflow mean and variability (Molnar et al., 2006; Lague, 2014; Rossi et al., 2016), which led to previous efforts to consider the influence of covarying mean and variability on long-term erosion efficiency (DiBiase & Whipple, 2011; Molnar et al., 2006). Previous work was based on empirical relationships. With our theoretical framework relating streamflow mean and variability index to climate and hydrology we are ideally suited to explore the effect of covarying, negatively correlated mean and variability index as a result of changing climate and hydrological boundary conditions.

We show the trajectory a river basin will chart in  $\mu$ - $\nu$  parameter space in response to changing climatic and hydrological boundary conditions using equation (25) (Figure 12). These trajectories tend to follow the negative correlation between mean and variability index (i.e., to trend from streamflow regimes with low mean and high variability index to regimes with high mean and low variability index). This dominant trend results in portions of  $\mu$ - $\nu$  space that are unlikely to be occupied by a river basin, because they require extreme climatic and hydrological conditions. This includes river basins with high mean and high variability index as well as rivers with low mean and low variability index, which corresponds to the upper right and lower left corners of the parameter space in Figure 12, respectively. This is useful for directing our analysis to a more restricted, realistic parameter space.

We compute the long-term erosion rate as a function of the streamflow mean and variability using equation (25) (shown as contours in Figure 12a, where  $b = 1.8$ ,  $q_{c*} = 5$ ,  $\gamma = 0.75$ ). Figures 12b and 12c show the absolute erosion rate along the corresponding trajectories in Figure 12a due to changing the mean storm frequency and intensity. These trajectories can result in a complex response to changing rainfall, such as dips and peaks in erosion rate due to the trade-off of streamflow mean and variability index. This is consistent with DiBiase & Whipple (2011, their Figure 10), who also find peaks in erosion rate for the same reason. For reference, we show the erosion rate for the CD-SPIM (no threshold or variability effects; equation (30) as well as a model where erosion rate is a simple function of mean rainfall (e.g.,  $\langle E \rangle = K \langle P \rangle^m S^n$ , Figures 12b and 12c). The reduction in variability index as mean streamflow increases reduces the impact of a higher mean streamflow relative to the CD-SPIM and direct rainfall SPIM. As a result, erosion is in many cases less efficient for high mean streamflow than predicted by simpler stream power models. This reiterates a point made by DiBiase

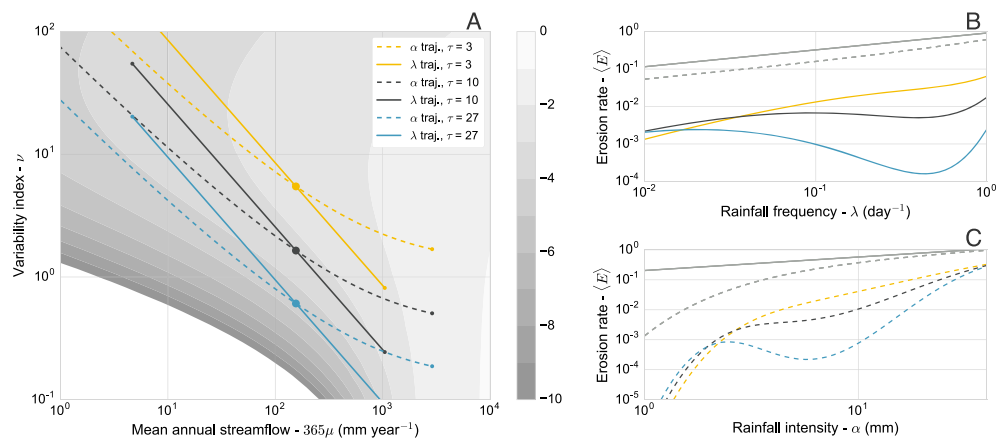


**Figure 12.** (a) River basins with the same hydrological conditions, but different hydrological response times, are shown as circles in the streamflow mean-variability index parameter space superimposed upon long-term erosion rate (grey contours; each contour represents an order of magnitude change in erosion rate). The trajectories that these basins follow with changing mean storm frequency (solid lines) and mean storm depth (dashed lines) are also plotted. (b) and (c) show the long-term erosion rate along the trajectories with the corresponding line color and style in (a). Also shown is the erosion rate as a function of rainfall intensity or frequency using the constant-discharge stream power incision model without threshold effects  $\langle E \rangle \propto \langle Q \rangle^{m_c}$  (dashed gray lines) and a simple mean rainfall stream power incision model  $\langle E \rangle \propto \langle P \rangle^{m_c}$  (solid gray lines). The erosion threshold is set at 5 times the mean streamflow ( $q_{c*} = 5$ ). As a consequence, the absolute magnitude of the threshold increases with increasing mean streamflow. Other hydroclimatic parameters:  $b = 1.8$ ,  $\gamma = 0.75$ ,  $PET = 10$  mm/d,  $s_o = 12$  mm.

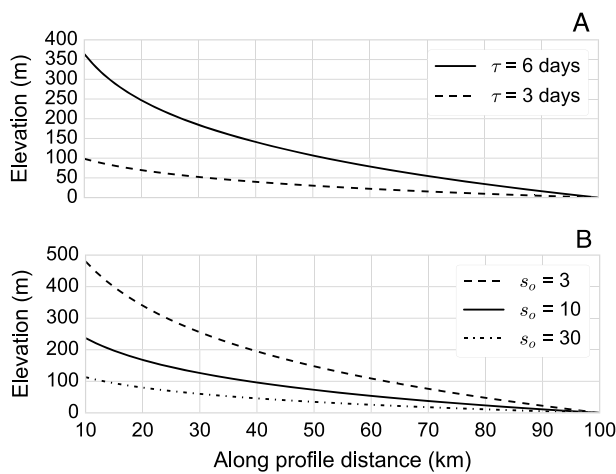
and Whipple (2011) that beyond a given mean streamflow, the long-term erosion rate is likely to become relatively insensitive to further increases in the mean streamflow. However, this is not true for the entire parameter space. We find, in contrast to DiBiase and Whipple (2011), that if the mean streamflow continues to increase, it eventually exceeds the erosion threshold so often that variability ceases to play a role, and erosion rates again increase. This is supported by empirical observations of Scherler et al. (2017). Finally, in general, rivers with a slower response time,  $\tau$  should be more significantly affected by the trade-off of streamflow mean and variability index.

Figure 12 illustrates why the changes in long-term erosion rate depend so heavily on both the climatic and hydrological conditions of the river basin. Even if it can be established that the trajectory a basin will follow with changing climatic forcing will trend from the lower right corner to the upper left corner of  $\mu$ - $\nu$  space, we cannot know how this will affect the erosion rate until we know the river basin's current position in  $\mu$ - $\nu$  space. This requires knowledge of both the climatic and hydrological conditions in that basin. Therefore, understanding what hydroclimatic regime a particular basin is in is key to understanding how the long-term erosion rate will respond to changes in climatic forcing.

#### 4.1.4. Critical Streamflow

Another key to understanding how the erosion rate will evolve with changing climate is the response of the erosion threshold. The critical streamflow is the minimum flow that exceeds critical shear stress needed for a given channel configuration (width, roughness, cross-sectional shape, and slope) (e.g., Lague et al., 2005; Tucker & Bras, 2000). As such it is influenced both by changes in channel hydraulics and critical shear stress. The parameterization of critical streamflow made here and in previous work (e.g., DiBiase & Whipple, 2011; Lague, 2014; Lague et al., 2005; Tucker, 2004; Tucker & Bras, 2000) assumes that narrower channels and/or steeper channels will be able to exceed the critical shear stress with lower streamflow magnitudes. Therefore, in steeper and/or narrower channel reaches, the role of thresholds and variability will be subdued relative to other parts of the channel network. However, sediment transport in steep channels is not as well studied as in alluvial channels from which the parameterization of  $q_{c*}$  was derived, and there may be other processes that reduce the dependence of  $q_{c*}$  on slope or width, such as a slope dependent Shields number (Lamb et al., 2008; Scherler et al., 2017).

Critical streamflow can also be influenced by changes in the critical shear stress. The critical shear stress is often related to the  $D_{50}$  of the grain size distribution in a river (DiBiase & Whipple, 2011; Lague et al., 2005).



**Figure 13.** Steady state river long profiles with an uplift rate of 0.5 mm/yr and constant climatic conditions. (a) Changes in the hydrologic response time,  $\tau$ , lead to long river profiles of different steepness due to the influence on streamflow variability which modify erosional efficiency. (b) Changes in the storage capacity also influence profile steepness, though the storage capacity influences both the mean and variability of streamflow. Modifying rainfall intensity, frequency, or evapotranspiration rates would have a similar effect.

There is evidence that the grain size distribution delivered from hillslopes to a river could be a function of erosion rate and climate (Attal et al., 2015; Sklar et al., 2017) in addition to lithology. If this is the case, and given the importance of the magnitude of critical streamflow, modeling the fluvial erosion response to large changes in climate as shown in Figure 12 may not be valid. Large climatic changes could have an impact on sediment availability and caliber that may amplify, reduce, or overshadow the change in streamflow mean or variability.

#### 4.2. Hydroclimatic Controls on Long Stream Profiles

To provide some tangible examples of the magnitude of influence of climatic and hydrological boundary conditions on the stream power model, we model the steady state long stream profile for several sets of different boundary conditions. We demonstrate with the following numerical experiments that reasonable changes in climatic and hydrological boundary conditions can result in significant changes in the erodibility rate constant  $K'$  and steepness exponent  $n$ . Unless otherwise noted, we use moderate values for all climatic and hydrological parameters:  $s_o = 3\text{--}30$  mm,  $PET = 10$  mm/d,  $\alpha = 10$  mm,  $\lambda = 0.6$  day<sup>-1</sup>,  $\bar{p} = 2$  mm/d, and  $\tau = 3\text{--}6$  days.

We first explore the effect of the hydrological response time. Rivers with shorter response times will be characterized by rapid streamflow responses to rainfall that have higher peak streamflows than rivers with

longer response times. In the model, this translates to a higher variability index, which should usually lead to more efficient fluvial erosion. River basins at steady state with short response times should have lower relief and smaller steepness indices than similar river basins with longer response times, all else equal.

This is borne out in Figure 13a, in which two river basins, identical except for the response time, are evolved to steady state. Changing the response time from 3 to 6 days, which is well within the observed range, results in a factor 3 change in relief. In our model, the hydrological response time is the sole parameter that influences the streamflow variability independent of the mean daily streamflow. Therefore, its impact may be overexaggerated here. However, its influence on the steady state long river profile is significant, suggesting that even if it is overexaggerated, the response time should be an important control on streamflow variability and fluvial erosion rates. Thus, the hydrologic response time, which can be an expression of tectonic history (i.e., fracturing), lithology, or basin size, could provide a mechanism for these basin properties to influence streamflow variability, and by extension, the steady state profile of rivers.

Differences in the aridity index,  $\phi$ , or the effective soil depth,  $s_*$ , between basins will have a similar effect as the response time. However, different to the hydrological response time, these nondimensional numbers control the runoff ratio, which influences both the mean and variability of streamflow. We explore this effect here by modifying the soil moisture storage capacity,  $s_o$ . However, differences in other controls on the aridity index or effective soil depth, such as the intensity or frequency of rainfall, or the mean evapotranspiration rate should have similar effects. We model three identical river basins, with the exception of  $s_o$ , which is varied from 3, to 10, to 30 mm (Figure 13b). For the chosen conditions this equates to effective soil depths of 0.3, 1, and 3, respectively. As a result the difference in soil storage capacity means that the basin with  $s_o = 3$  is in the thin, dry soil regime, while the basin with  $s_o = 30$  is in the thick, dry soil regime. This has significant consequences for the runoff ratio, resulting in different streamflow means and variability indices between the three basins and different steady state river profiles.

#### 4.3. The Failure to Find Trends Between Rainfall Rates and Erosion Rates

Regional comparisons of mean rainfall rates to long-term erosion rates often fail to find significant correlation between the two (e.g., Acosta et al., 2015; Bermudez et al., 2012; Blanckenburg, 2005; Burbank et al., 2003; Godard et al., 2014; Riebe et al., 2001). This is perhaps not surprising as there are several confounding factors such as river slope, catchment area, and spatially varying lithology and uplift rate. In general, comparisons of the steepness index against long-term erosion rates yield clearer trends (DiBiase & Whipple, 2011; DiBiase et al., 2010; Wobus et al., 2006); however, they still exhibit considerable spread. Spatially varying lithologies can be responsible for this spread, but spatial variation of climatic and hydrological boundary conditions

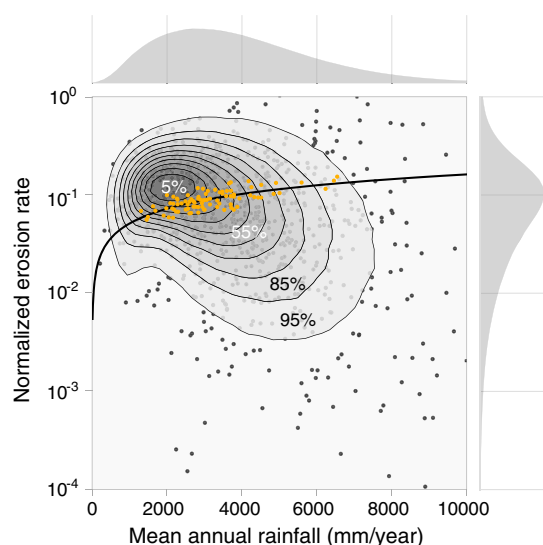


**Figure 14.** The distribution of two million Monte Carlo simulations of the long-term erosion rate for a wide range of hydrological and climatic conditions plotted against normalized erosion rate. Contours encompass given percentage of all simulations, in 10% steps. Additionally, we have shown a small subsample of the simulations as black dots. The trend of the normalized erosion rate for a selected set of hydroclimatic parameters according to equation (25) is shown a black line; the simulations with parameters falling with  $\pm 10\%$  of the selected set are shown as yellow points.

( $b$ ,  $\tau$ ,  $\phi$ ,  $s_*$ ) can also cause this spread. It should be expected that comparisons of mean rainfall rate, specific stream power, or channel steepness index against the long-term erosion rate over large regions of the Earth do not yield a clear relationship, even when the landscape is expected to be at steady state and the spatial distribution of uplift rate is known and accounted for. Different hydrological conditions can give rise to different fluvial responses to the same climatic forcing, and therefore different long-term erosion rates.

This is demonstrated by the results of 2 million Monte Carlo simulations of the long-term erosion rate are shown for a wide range of hydrological and climatic conditions (Figure 14). The river slope  $S$ , catchment area  $A$ , erodibility coefficient  $K$ , and the exponents  $n$  and  $m$  were held constant. The long-term erosion rate can be seen to vary by several orders of magnitude for a given rainfall rate. This is mostly due to variations in streamflow ratio,  $\omega$ , the streamflow variability (parameterized by  $b$  and  $\nu$ ), the erosion threshold,  $q_{c*}$  and the erosion nonlinearity,  $\gamma$ . This illustrates how spatially and temporally varying hydrological, climatic, and channel conditions can obfuscate the relationship between mean rainfall rate and the long-term erosion rate. However, a trend between mean annual rainfall rate and the erosion rate emerges from the Monte Carlo simulations when just these five important controls are taken into consideration (yellow points in Figure 14).

The implication is that the failure of many studies to find regional trends in erosion rate correlated to mean rainfall rate or stream power does not necessarily point to a dominance of tectonics over climate. It could also reflect the fact that not all of the important factors determining how rainfall drives erosion in a fluvially dominated landscape have been taken into account.

#### 4.4. Outstanding Issues and Limitations

##### 4.4.1. Climate and Hydrological Nonstationarity

In this study we have chosen daily rainfall to represent the variability in climate and study how it affects mean erosion rate which evolves over much longer timescales.

The resulting difference in timescales between the forcing (rainfall) and the response (erosion) is significant. While a stochastic approach is useful to upscale these daily processes to landscape evolution timescales, it assumes that the climatic and hydrological conditions are stationary—that they do not change over long periods of time. However, it is clear that climate does in general change consistently over periods as short as decades to centuries. Some of the key parameters, such as the streamflow ratio  $\omega$ , streamflow variability  $\nu$ , and recession exponent  $b$  are relatively straightforward to measure in present-day basins (Doulatyari et al., 2015). However, there is the inevitable question of whether or not these values have any meaning over geological time.

It is common in applications of the hydrology model to break the year into seasons over which the controls on the pdf of streamflow are constant (Doulatyari et al., 2015), as was also found to be necessary by Scherler et al. (2017) who break the Himalayan year into the monsoon season and the dry season. This suggests a single season as a minimum time step for any landscape evolution model based on this theory. However, it should be possible to take larger time steps by using a composite streamflow pdf made of seasonal distributions weighted by the length of the season, again an approach taken by Scherler et al. (2017). In that case the time step is constrained by the period over which seasonal controls on the probability distribution of streamflow remain relatively constant. It most places at most times it is probably reasonable to expect to be able to use time steps on the order of one to a few decades (e.g., Botter, 2014; Botter et al., 2013), though more research on reasonable time steps is warranted. Much more challenging than ensuring stationarity of hydroclimatic conditions over a single time step will be deciding how to evolve these controls over time.

##### 4.4.2. Catchment-Scale Parameters

The model presented here is purposely minimalistic. It reflects an effort to simply capture the key behaviors of complex nonlinear systems while retaining low dimensionality. A result of this is that the presented framework makes use of spatially integrated catchment-scale parameters, with the implicit assumption that a single value can be used to represent spatially heterogeneous local, or point-scale, parameters. This produces a challenge. It is not always clear how the behavior at the point-scale relates to a catchment-scale parameter. For example,

although the mean rainfall rate at the catchment-scale is simply the arithmetic mean of the point-scale mean rainfall rates, the same is not true for the mean storm depth or the mean storm frequency. An understanding of how the point-scale parameters relate to the catchment-scale parameters, either empirical or theoretical, is needed to extend this work to 2-D landscape evolution models.

#### 4.4.3. Heavy-Tailed Rainfall

There are three important statistical characteristics of daily rainfall in the context of fluvial erosion rates. The mean storm depth, the mean storm frequency, and the heaviness of the tail of the distribution of rainfall. In this work, we use an exponential distribution for daily rainfall that prohibits exploring the effects of a heavier tail. The exponential distribution is known to be imperfect for modeling daily distributions of storm depths, because it is often lighter tailed than empirical rainfall distributions. However, the stochastic nature of rainfall is still captured, with the exponential distribution approximating the strongly right skewed magnitude-frequency structure observed in nature while exhibiting the key memoryless property that makes it analytically tractable. It has been shown that there are no true analytical solutions for the probability distribution of soil moisture, and therefore for the probability distributions of daily streamflow and erosion for other functions commonly used to represent daily rainfall, such as the gamma distribution (Verma et al., 2011).

Mueller et al. (2014) tested numerically the error in the estimated distribution of daily streamflow produced by using an exponential distribution to represent rainfall and found it to be a poor assumption only in the case of heavy-tailed storm depth distributions (gamma shape parameter  $< 0.5$ ). While there is some evidence that the heaviness of the tail of rainfall is important in arid regions (Daly & Porporato, 2010; Mueller et al., 2014), Rossi et al. (2016) presented an empirical analysis that suggests it is only a secondary control on the distribution of daily streamflow. We feel that the uncertainties in other parts of the derivation, mainly the streamflow-erosion relation preclude the need to focus on the details of rainfall. The fact that the exponential model of storm depths captures the highly right skewed nature of rainfall distributions is sufficient. Additionally, we find the benefits of analytical solutions make the exponential distribution a worthwhile choice for daily storm depth.

#### 4.4.4. Limitations of the Stream Power Approach

The stream power approach used in this study is limited in that it does not allow for sediment transport dynamics to be modeled at all and does not work well on short timescales (Beer & Turowski, 2015). The hydrological model outlined above could be integrated with a more sophisticated model of fluvial erosion. However, the stream power approach remains popular because it successfully predicts many aspects of the steady state long river profile (Lague, 2014). Further, as pointed out by DiBiase and Whipple (2011) at steady state it is not possible to distinguish between the stream power model and sediment transport driven models. We have chosen to use the stream power approach because its simplicity enhances clarity in an already complex analysis, which is useful for a first step. It also allows us to compare our results with previous results and provides a standard for future analysis using a more sophisticated erosion model.

Future fluvial incision models will invariably depend to some degree on instantaneous streamflow. Further, Lague, (2010, 2014) have convincingly demonstrated that upscaling these models temporally is a critical step that can modify the form of equations substantially. Stochastic hydrological models such as the one used here provide a powerful tool to properly upscale incision models to long timescales while simultaneously linking the long-term behavior to climatic and hydrological boundary conditions. The usefulness of this approach is not limited to the SPIM.

## 5. Conclusions

We have developed a theoretical framework for long-term fluvial erosion rates based on a stochastic-mechanistic model of hydrology in the context of the SPIM. This theory points to six important controls: (1) the statistics of rainfall, described by the mean storm depth  $\alpha$  and frequency  $\lambda$ ; (2) soil and vegetation dynamics which modify incoming rainfall, described here by aridity index  $\phi$ , the effective soil storage capacity  $s_*$  and the streamflow ratio  $\omega$ ; (3) basin response to input described by the hydrological response time  $\tau$  and the nonlinearity of the response  $b$  to forcing; (4) the erosion threshold,  $q_{c*}$ ; (5) the nonlinearity of the daily streamflow-erosion relationship,  $\gamma$ ; and (6) the stream power parameters (the exponents  $m$  and  $n$ , the erodibility coefficient  $K$ , and the river slope  $S$ ). The first three controls determine the distribution of daily streamflow (essentially by setting  $\mu$ ,  $\nu$  and  $b$ ), and the last three controls determine how that distribution of streamflow relates to the distribution of daily erosion and the mean long-term erosion rate. This highlights the two necessary aspects of any climate driven fluvial erosion model: a model for how rainfall translates into

streamflow, and a model for how streamflow drives fluvial erosion. The framework presented here allows for a large range of daily streamflow regimes and makes use of a general daily streamflow-erosion model (a power law with a threshold and an exponent that can be less than or greater than one). Therefore, we expect that the main conclusions laid out here will generally apply, even when compared to models with more sophisticated hydrological or streamflow-erosion laws.

We defined a daily streamflow variability index that it is applicable to a wide range of hydrological regimes and established that it has a solid physical basis. We also provided a theoretical basis for why streamflow variability is negatively correlated with mean daily streamflow, a long-observed relationship which is useful for determining the erosional response to changing climate in a threshold-stochastic stream power context. Furthermore, by using the hydrological model to relate both the mean and variability of streamflow to the climatic and hydrological boundary conditions, we show how fluvial erosion might respond to realistic climatic forcing. This allows for direct comparison to meteorological, hydrological, and geomorphological observations.

Finally, we demonstrated that the hydrological conditions in a river basin and the threshold-stochastic nature of the streamflow-erosion relationship can cause the long-term erosion rate to vary over several orders of magnitude for a given mean annual rainfall or streamflow rate. The failure of prior studies to find a dependence of erosion rate on mean annual rainfall or streamflow may stem from not taking into account the above effects.

## Notation

- $\lambda$  ( $s^{-1}$ ) Mean frequency of daily rainfall. Equivalent to fraction of days with rainfall.
- $p$  (m) Random variable representing specific rainfall intensity, measured as mean depth of daily rainfall over river catchment.
- $\alpha$  (m) Specific rainfall intensity, measured as mean depth of daily rainfall over river catchment. This is the mean magnitude of daily rainfall on days with rainfall.
- $f_p(p)$  The pdf of daily rainfall intensity.
- $\bar{p}$  ( $m s^{-1}$ ) Specific mean daily rainfall rate, measured as mean depth of rainfall over river catchment. In contrast to mean daily rainfall intensity, this is the mean rainfall rate including days with no rainfall.
- $n_{sol}$  ( $0 \leq n_s \leq 1$ ) (nondimensional) Soil porosity (i.e., fraction of soil volume not occupied by soil).
- $Z_r$  (m) Vertical thickness of soil/active layer/rooting depth.
- $s$  ( $0 \leq s \leq 1$ ) (nondimensional) Random variable representing soil moisture (0 is no soil moisture, 1 is completely saturated).
- $s_w$  ( $0 < s_w < s_1$ ) (nondimensional) Wilting point—soil moisture threshold below which transpiration by plants ceases, and evapotranspiration rates are low. Here evapotranspiration is assumed to stop completely below this threshold.
- $s_1$  ( $s_w < s_1 < 1$ ) (nondimensional) Soil moisture threshold at which significant streamflow generation occurs.
- $s_o$  (m) The dynamic soil moisture capacity (e.g., depth of rainfall per unit area that can be absorbed by soil layer).  $s_o = (s_1 - s_w)n_s Z_r$ .
- $\omega$  [ $0 \leq \omega \leq 1$ ] (nondimensional) Runoff ratio. The fraction of incoming rainfall that is partitioned into streamflow.
- $\phi$  (nondimensional) Aridity index. Ratio of potential evapotranspiration rate to mean rainfall rate.
- $s_*$  (nondimensional) Effective soil depth. Ratio of soil storage capacity to mean storm depth.
- PET ( $m s^{-1}$ ) Maximum evapotranspiration rate.
- $\langle ET \rangle$  ( $m^3 s^{-1}$ ) Mean long-term, catchment integrated rate of loss of water to evapotranspiration.
- $\langle P \rangle$  ( $m^3 s^{-1}$ ) Mean long-term, catchment integrated rate of gain of water from precipitation.
- $\langle Q \rangle$  ( $m^3 s^{-1}$ ) Mean long-term, catchment integrated rate of loss of water to streamflow.
- $W$  (m) Catchment-scale water storage normalized by catchment area.
- $q$  (m) Random variable representing specific daily streamflow magnitude.
- $c_w$  Coefficient of storage-streamflow power law.
- $d$  (nondimensional) Exponent of storage-streamflow power law.
- $a$  ( $m^{b-1} s^{b-2}$ ) Recession coefficient.
- $b$  (nondimensional) Recession exponent.
- $\xi_r$  ( $m s^{-2}$ ) Stochastic effective rainfall forcing.
- $\tau$  ( $s^{-1}$ ) Hydrologic response time.

- $\tau_{\text{storm}}$  ( $\text{s}^{-1}$ ) Mean time between runoff generating storms (floods).  $\tau_{\text{storm}} = 1/\omega\lambda$ .
- $\nu$  (nondimensional) Streamflow variability index. Related to inverse of parameter used to describe variability in previous work ( $\nu = 1/k$ ).  $\nu = \tau_{\text{storm}}/\tau = (\omega\lambda\tau)^{-1}$ .
- $\beta$  Rate parameter in distributions of streamflow.
- $k$  (nondimensional) Parameter used to describe variability in previous work, related to variability index ( $k = 1/\nu$ ).  $k = \tau/\tau_{\text{storm}} = \omega\lambda\tau$ .
- $q_0$  ( $\text{m s}^{-1}$ ) Scaling factor used to decorrelate recession coefficient  $a$ . Here it is taken as being equal to the specific mean daily streamflow.
- $\mu$  ( $\text{m s}^{-1}$ ) Specific mean daily streamflow.
- $\hat{a}$  ( $\text{s}^{-1}$ ) Decorrelated recession coefficient.  $\hat{a} = a\mu^{b-1}$ .
- $q_*$  (nondimensional) Random variable representing normalized daily streamflow.  $q_* = q/\mu$ .
- $f_{Q_*}(q_*)$  The pdf of normalized daily streamflow.
- $f_Q(q)$  The pdf of daily streamflow.
- $C$  Normalizing constant for pdf of daily streamflow when  $b \neq 1$  or  $2$ .
- $p_0$  Atom of probability that  $q = 0$  when  $b < 1$ .
- $a_t$  (nondimensional) Exponent of shear stress erosion law.
- $k_e$  ( $\text{m s}^{-1} \text{Pa}^{-a_t}$ ) Rate constant of shear stress erosion law describing efficiency of erosion.
- $\tau_s$  (Pa) Shear stress on river bottom exerted by streamflow.
- $\tau_c$  (Pa) Critical shear stress for erosion to take place.
- $\epsilon$  ( $\text{m s}^{-1}$ ) Daily fluvial erosion rate.
- $K$  ( $\text{m}^{(1-3m_c)} \text{s}^{-(1+m_c)}$ ) Erodibility constant,  $K = k_e k_t^{a_t} k_w^{-a_t a_t}$ .
- $A$  ( $\text{m}^2$ ) Catchment area.
- $S$  (nondimensional) Slope of river channel.
- $m$  (nondimensional) Stream power area exponent.
- $m_c$  (nondimensional) Area exponent in CD-SPIM,  $m_c = a_t \alpha_t (1 - \omega_b)$ .
- $m_s$  (nondimensional) Area exponent in TS-SPIM,  $m_s = \frac{m_c}{\gamma} \left( \frac{q_c^{2-b}}{\nu} + 1 \right)$ .
- $n$  (nondimensional) Stream power steepness or slope exponent.
- $n_c$  (nondimensional) Steepness exponent in CD-SPIM,  $n_c = a_t \beta_t$ .
- $n_s$  (nondimensional) Steepness exponent in TS-SPIM,  $n_s = \frac{n_c}{\gamma} \left( \frac{q_c^{2-b}}{\nu} + 1 \right)$ .
- $\psi$  ( $\text{m s}^{-1}$ ) Erosion threshold,  $\psi = k_e t_c^{a_t}$ .
- $\gamma$  (nondimensional) Daily stream power exponent describing the at-a-station nonlinearity of fluvial erosion as a function of daily streamflow.
- $q_c$  ( $\text{m s}^{-1}$ ) Specific critical streamflow value that exceeds critical shear stress threshold for a given mean streamflow, and channel slope and cross-sectional shape.
- $q_{c*}$  (nondimensional) Normalized critical streamflow value.  $q_{c*} = q_c/\mu$ .
- $q_m$  ( $\text{m s}^{-1}$ ) Maximum daily specific streamflow observed.
- $q_{m*}$  (nondimensional) Normalized maximum daily streamflow.  $q_{m*} = q_m/\mu$ .
- $\langle E \rangle$  ( $\text{m s}^{-1}$ ) Mean fluvial erosion rate.
- $\lambda_\epsilon$  (nondimensional) Mean frequency of fluvial erosion.
- $\mu_\epsilon$  (nondimensional) Nonlinear average of fluvial erosion weighted by  $\gamma$ .
- $\alpha_t$  (nondimensional) Flow exponent from Darcy-Weisbach ( $\alpha_t = 2/3$ ) or Gauckler-Manning-Strickler ( $\alpha_t = 3/5$ ) flow resistance relationship.
- $\beta_t$  (nondimensional) Slope exponent from Darcy-Weisbach ( $\beta_t = 2/3$ ) or Gauckler-Manning-Strickler ( $\beta_t = 7/10$ ) flow resistance relationship.
- $\omega_s$  (nondimensional) Exponent controlling at-a-station scaling of flow width with instantaneous streamflow magnitude.
- $\omega_b$  (nondimensional) Empirically derived exponent describing along channel scaling of flow width with mean streamflow magnitude.
- $k_t$  ( $\text{Pa s}^\alpha \text{m}^{(-2\alpha)}$ ) Rate coefficient from Darcy-Weisbach or Gauckler-Manning-Strickler flow resistance relationship.
- $k_w$  ( $\text{m}^{(1-3\omega_b)} \text{s}^{(\omega_b)}$ ) Empirically derived rate coefficient describing along channel scaling of flow width with mean streamflow magnitude.
- $K'$  ( $\text{m}^{1-2n} \frac{m_c}{n_c} \text{s}^{-1}$ ) SPIM rate constant relating mean long-term erosion rate to steepness index, it is independent of steepness index.

$K_{cd}$  ( $m^{1-2m_c} s^{-1}$ ) CD-SPIM rate constant relating mean long-term erosion rate to steepness index, it is independent of steepness index.

$K_{ts}$  ( $m^{1-2m_s} s^{-1}$ ) TS-SPIM rate constant relating mean long-term erosion rate to steepness index, it is independent of steepness index.

$k_s$  ( $m^{2n \frac{m_c}{n_c}}$ ) Steepness index, a measure of area normalized channel slope,  $k_s = A^\theta S$ .

$\theta$  (nondimensional) Concavity index  $\theta = \frac{m_c}{n_c} = \frac{\alpha_t}{\beta_t} (1 - \omega_b)$ .

### Appendix A: Special Functions

In this study we use the upper regularized incomplete gamma function  $\Gamma(\cdot)$  defined as

$$\Gamma(s, x) = \frac{1}{\Gamma(s)} \int_x^\infty t^{s-1} e^{-t} dt, \tag{A1}$$

where  $\Gamma(\cdot)$  is the gamma function, defined as

$$\Gamma(s) = \int_0^\infty t^{s-1} e^{-t} dt. \tag{A2}$$

We also use the lower regularized incomplete gamma function  $\gamma(\cdot)$  defined as

$$\gamma(s, x) = 1 - \Gamma(s, x) = \frac{1}{\Gamma(s)} \int_0^x t^{s-1} e^{-t} dt. \tag{A3}$$

We made a point to use only the regularized versions of the incomplete gamma function even though this made the notation a bit more awkward because they are simpler to call in python and Matlab. In python these functions as used here can be called using the scipy package as follows: the gamma function as `scipy.special.gamma(s)`; the upper regularized incomplete gamma function as `scipy.special.gammaincc(s,x)`; and the lower regularized incomplete gamma function as `scipy.special.gammainc(s,x)`. In Matlab these functions as used here can be called as follows: the gamma function as `gamma(s)`; the upper regularized incomplete gamma function as `gammainc(x,s,'upper')`; and the lower regularized incomplete gamma function as `gammainc(x,s,'lower')`, or simply as `gammainc(x,s)`.

Further, we make use of modified Bessel functions of the second kind (Veling, 2011), defined here as

$$K_\nu(s) = \frac{2^{\nu-1}}{s^\nu} \int_0^\infty t^{\nu-1} e^{-\left(t + \frac{s^2}{4t}\right)} dt, \tag{A4}$$

which can be called in python as `scipy.special.kv(v,s)`.

Finally, we use the generalized gamma function (Harris, 2008; Veling, 2011), which is defined as

$$\Gamma(s, x; a) = \int_x^\infty t^{s-1} e^{-\left(t + \frac{a}{t}\right)} dt. \tag{A5}$$

Note that  $\Gamma(s, x; 0) = \Gamma(s, x)$  and  $\Gamma(s, 0; 0) = \Gamma(s)$ . Also, a useful identity is

$$\Gamma(s, 0; a) = 2a^{s/2} K_s(2\sqrt{a}), \tag{A6}$$

where  $K_s(\cdot)$  is the modified Bessel function defined above. We use this to define a generalized upper regularized incomplete gamma function that is analogous to the incomplete regularized functions above

$$\Gamma_g(s, x; a) = \frac{1}{\Gamma(s, 0; a)} \int_x^\infty t^{s-1} e^{-\left(t + \frac{a}{t}\right)} dt = \frac{1}{2a^{s/2} K_s(2\sqrt{a})} \int_x^\infty t^{s-1} e^{-\left(t + \frac{a}{t}\right)} dt. \tag{A7}$$

### Appendix B: Distribution of Daily Streamflow When $b = 2$

Botter et al. (2009) showed that the pdf of  $q$  is

$$f_Q(q) = C \frac{dr(q)/dq}{q} \exp \left[ -\frac{r(q)}{\alpha} + \omega \lambda \int g(r(q))^{-1} dr(q) \right] + p_o \delta(q), \tag{B1}$$

where  $C$  is a normalizing constant,  $p_o\delta(q)$  is an atom of probability that  $q = 0$ ,  $g(x)$  is the storage loss function  $q = g(W)$ , and  $r(q)$  is its inverse

$$W = g^{-1}(q) = r(q). \tag{B2}$$

To find  $r(q)$  in the case  $b = 2$ , we start with

$$\frac{dq}{dt} = -aq^2. \tag{B3}$$

We also note that due to conservation of mass, the storage term  $W$  will change over time as

$$\frac{dW}{dt} = -q. \tag{B4}$$

Integrating both (B3) and (B4), it is straightforward to show that (with the assumption that  $q(0) = 0$ )

$$q(t) = (at)^{-1} \tag{B5}$$

and

$$W(t) = -\frac{1}{a}\ln(t) + c. \tag{B6}$$

Inverting (B5) and substituting it into (B6) leads to

$$r(q) = \frac{1}{a}\ln(cq), \tag{B7}$$

where  $c$  is a constant. Putting  $r(q)$  into the general solution for the pdf of daily stream flow (equation (B1)), we find that for  $b = 2$

$$f_Q(q) = \frac{(\omega\lambda/a)^{1/\alpha\alpha+1}}{\Gamma(1/\alpha\alpha+1)} q^{-1/\alpha\alpha-2} \exp[-\omega\lambda/aq], \tag{B8}$$

which is an inverse gamma function equivalent to equation (9) when the substitution  $a = \mu^{1-b}/\tau$  is made.

### Appendix C: Analytical Approximations for C

We can rewrite the general distribution of daily streamflow (equation (10)) as

$$f_{Q_*}(q_*) = Cq_*^{-b} e^{-k_1q_*^{1-b}} e^{k_2q_*^{2-b}}, \tag{C1}$$

where  $k_1 = k/(b - 1)$  and  $k_2 = k/(b - 2)$ . To find  $C$ , we need to integrate from 0 to  $\infty$

$$C = \left[ \int_0^\infty q_*^{-b} e^{-k_1q_*^{1-b}} e^{k_2q_*^{2-b}} dq_* \right]^{-1}. \tag{C2}$$

If we make the substitution  $t = x^{1-b}$  and  $dt = (1 - b)x^{-b}dx$

$$C = \frac{(1 - b)}{\int_0^\infty e^{k_2t^\phi} e^{-k_1t} dt}, \tag{C3}$$

where  $\phi = -k_1/k_2 = (b-2)/(1-b)$ . This is equivalent to the laplace transform of the first term of the integrand

$$C = \frac{(1 - b)}{\mathcal{L}\{e^{k_2t^\phi}\}(k_1)}. \tag{C4}$$

This is the laplace transform of a stretched exponential, and there is no simple analytical solution, though solutions in the form of Meijer G functions are possible for certain values of  $b$ , as well as simpler solutions for particular values of  $b$ , such as  $b = 3/2$ . We also offer one approximation, valid only for  $1 < b < 2$ , arrived

at by noting the similarity between equations (8)–(10), and by taking advantage of the known normalizing factors from equations (8) and (9)

$$C = \left( \frac{2\pi(2-b)(b-1)}{\mu^2 k} \right)^{1/2} \frac{(k/(2-b))^{k/(2-b)}}{\Gamma(k/(2-b))} \frac{k/(b-1)^{k/(b-1)}}{\Gamma(k/(b-1))}. \quad (C5)$$

This approximation has very low error when  $k > 1$ . When  $k < 1$ , the error is low when  $b$  is close to 1 or 2 and reaches a maximum when  $b = 1.5$ . The error reaches about 50% for  $b = 1.5$  when  $k = 0.01$ .

## Appendix D: Channel Hydraulics

A common starting point for derivations of the stream power law is given by Tucker (2004) and Lague et al. (2005)

$$\varepsilon = k_e (\tau_s^{\alpha_t} - \tau_c^{\alpha_t}), \quad \tau_s > \tau_c, \quad (D1)$$

which relates the daily fluvial incision rate  $\varepsilon$  to the excess shear stress on the riverbed. The exponent  $\alpha_t$  is a function of dominant incision process (Whipple et al., 2000), and the rate coefficient  $k_e$  appears to be in the range of  $10^{-13}$  (Lague, 2014). In order to make use of the distribution of daily streamflow, it is necessary to relate the streamflow to the shear stress it exerts. To do this, we use the derivation of Tucker and Bras (2000) to relate the shear stress exerted on the riverbed to the flow depth (approximated by the streamflow  $qA$  divided by the river width) and the riverbed slope using a formulation equivalent to the Manning or Darcy-Weisbach equation, depending on the values for  $\alpha_t$  and  $\beta_t$ ,

$$\tau_s = k_t \left( \frac{qA}{w} \right)^{\alpha_t} S^{\beta_t}, \quad (D2)$$

where  $w$  is the channel width,  $S$  is the riverbed slope, and  $k_t$  is a factor accounting for acceleration of gravity, density of water, and a friction factor. This implies that what we need to know in order to estimate the shear stress  $\tau_s$  from the distribution of streamflow is the relationship between stage (the height of water surface) and streamflow. Tucker and Bras (2000), Lague et al. (2005), and DiBiase and Whipple (2011) accomplish this with two empirical relations. First, they describe how the width of the river at one location on the river changes relative to a benchmark width (e.g., bankfull width or mean streamflow width) with daily variations in streamflow,

$$\frac{w}{w_a} = \left( \frac{q}{\mu} \right)^{\omega_s}, \quad (D3)$$

where  $w_a$  is the benchmark width. This amounts to describing the cross-sectional profile of the channel. Different shapes can be described by changing the value of  $\omega_s$ . Lague et al. (2005) then describe how the benchmark width of the river increases with downstream increases in  $\langle Q \rangle$ , written as a power law

$$w_a = k_w \langle Q \rangle^{\omega_b}, \quad (D4)$$

where  $k_w$  and  $\omega_b$  are empirically derived constants.

Substituting equations (D2)–(D4) into (D1) leads to equation (20), which describes the daily erosion rate in terms of daily streamflow and river slope

$$\varepsilon = K \langle Q \rangle^{m_c} S^{n_c} q_*^\gamma - \psi, \quad q > q_c, \quad (D5)$$

where  $K = k_e k_t^{\alpha_t} k_w^{-\alpha_t \omega_b}$ ,  $m_c = \alpha_t \alpha_t (1 - \omega_b)$ ,  $n_c = \alpha_t \beta_t$ ,  $\gamma = \alpha_t \alpha_s (1 - \omega_s)$ , and  $\psi = k_e \tau_c^{\alpha_t}$  (Lague et al., 2005; Tucker & Bras, 2000).

## Appendix E: Missing Probability in Previous Approaches to Estimating Long-Term Fluvial Erosion Rates

To obtain the long-term mean erosion rate, previous studies integrated the magnitude of daily incision as a function of streamflow, weighted by the probability of observing a particular streamflow magnitude (e.g., DiBiase & Whipple, 2011; Huang & Niemann, 2006b; Lague et al., 2005; Tucker & Bras, 2000)

$$\langle E \rangle = \int_{q_c^*}^{q_{m^*}} \varepsilon(q_*) f_{Q_*}(q_*) dq_*, \quad (E1)$$

where the lower bound of the integral is the critical streamflow that exceeds the erosion threshold and the upper bound is the maximum streamflow expected in the period of observation. Conceptually, this approach makes sense, though mathematically, there is a small problem.

The probability of erosion not occurring plus erosion occurring accounts for all possible outcomes, and therefore must be equal to one ( $\int_0^\infty f_{Q_*}(q_*)dq_* = 1$ ). The probability of erosion not occurring is equal to the probability that streamflow does not exceed the critical streamflow,  $Pr[q_* < q_{c*}] = \int_0^{q_{c*}} f_{Q_*}(q_*)dq_*$ . In equation (E1), the probability that erosion occurs is implicitly stated to be  $Pr[q_{c*} \leq q_* \leq q_{m*}] = \int_{q_{c*}}^{q_{m*}} f_{Q_*}(q_*)dq_*$ . There is a small probability remaining that  $q_* > q_{m*}$ . Simply stating that streamflow should not exceed the maximum is not sufficient. Equation (E1) implicitly, and accidentally, assumes that when streamflow exceeds the maximum  $q_{m*}$  no erosion occurs. The assumption that should be made is that the probability of exceeding the maximum streamflow is zero. This requires truncating the streamflow pdf above  $q_{m*}$  before integrating, leading to a slightly modified pdf,  $f_{Q_*}^t(q_* | q_{m*})$ . Finally, and most importantly, this pdf is renormalized such that the  $Pr[q_* < q_{m*}] = 1$  (Daly & Porporato, 2010).

In most cases, this is not a significant issue, because the probability of exceeding the maximum streamflow is low. However, when the distribution of streamflow is highly variable, or the maximum streamflow is chosen to be relatively small, the missing probability will be more significant, which can lead to incorrect estimations of the long-term erosion rate. To correct this, it is possible to take the same approach as previous studies, but now integrating to infinity and using a properly truncated pdf of streamflow  $f_{Q_*}^t(q_* | q_{m*})$  (see Appendix F for derivation of truncated pdf)

$$\langle E \rangle = \int_{q_{c*}}^{\infty} \varepsilon(q_*) f_{Q_*}^t(q_* | q_{m*}) dq_* \quad (E2)$$

However, we use a different approach described in the next appendix that is functionally equivalent but we feel is more complete and provides a firmer theoretical basis for future work.

## Appendix F: Long-Term Erosion Rate

### F1. Pdf of Daily Erosion

We start with the distributions of streamflow for  $b = 1$

$$f_{Q_*}(q_*) = \frac{k^k}{\Gamma(k)} q_*^{k-1} \exp[-kq_*] \quad (F1)$$

$b = 2$

$$f_{Q_*}(q_*) = \frac{k^k}{\Gamma(k)} q_*^{k-2} \exp[-kq_*^{-1}] \quad (F2)$$

and  $b \neq 1, 2$

$$f_{Q_*}(q_*) = C q_*^{-b} \exp\left[-k\left(\frac{q_*^{2-b}}{2-b} - \frac{q_*^{1-b}}{1-b}\right)\right] \quad (F3)$$

Imposing a maximum observed daily streamflow  $q_{m*}$  truncates the pdf above  $q_{m*}$  and requires that the pdf be renormalized such that  $\int_0^{q_{m*}} f_{Q_*}(q_*)dq_* = 1$ . This leads to a new distribution  $f_{Q_*}^t(q_* | q_{m*})$

$$f_{Q_*}^t(q_* | q_{m*}) = \begin{cases} C f_{Q_*}(q_*) & q_* \leq q_{m*} \\ 0 & q_* > q_{m*} \end{cases}, \quad (F4)$$

where  $C$  is a normalizing constant. We can find this constant by integrating  $f_{Q_*}^t(q_* | q_{m*})$ :

$$\int_0^\infty f_{Q_*}^t(q_* | q_{m*})dq_* = C \left( \int_0^{q_{m*}} f_{Q_*}(q_*)dq_* + \int_{q_{m*}}^\infty 0 dq_* \right) = 1, \quad (F5)$$

which, in the case of  $b = 1$ , leads to

$$C = [1 - \Gamma(k, kq_{m*})]^{-1} \quad (F6)$$

and in the case  $b = 2$

$$C = \Gamma(k + 1, k/q_{m*})^{-1}, \tag{F7}$$

where  $\Gamma(a, x)$  is the regularized upper incomplete gamma function.

The effect of a threshold at  $q_* = q_{c*}$  is different than truncating the pdf because we gather the probability of  $q_* < q_{c*}$  into an atom of probability in the pdf of  $\epsilon$  at  $\epsilon = 0$ . This atom of probability is equal to  $Pr[q_* < q_{c*}]$ . We define this atom of probability as  $1 - \lambda_\epsilon$ . The probability that an erosion event occurs then is  $\lambda_\epsilon$ , defined in the text.

If we assume a relationship between daily incision  $\epsilon$  and daily streamflow  $q$  of the form  $\epsilon = g(q)$ , then we can calculate the pdf of daily incision as a simple change of variable

$$f_E(\epsilon) = f_Q^t(g^{-1}(\epsilon) | q_m) \frac{dq}{d\epsilon}. \tag{F8}$$

So then the overall pdf of  $\epsilon$  is composed of three parts. First, the atom of probability at  $\epsilon = 0$ , second, the truncated probability distribution of  $q > q_c$  as a function of  $\epsilon$ , and finally, 0 for all values of  $\epsilon$  corresponding to  $q > q_m$  because the probability of  $q > q_m$  is also 0:

$$f_E(\epsilon) = \begin{cases} 1 - \lambda_\epsilon & \epsilon = 0 \\ \lambda_\epsilon f_Q^t(g^{-1}(\epsilon) | q_m) & 0 < \epsilon \leq \epsilon_m \\ 0 & \epsilon > \epsilon_m \end{cases}, \tag{F9}$$

where  $\epsilon_m = \epsilon(q_m)$ .

If we want to use the pdf of daily incision to calculate the long-term erosion rate, we simply calculate the mean incision rate

$$\langle E \rangle = \int_0^\infty \epsilon f_E(\epsilon) d\epsilon, \tag{F10}$$

which, using the definition of  $f_E(\epsilon)$ , breaks down to

$$\langle E \rangle = \epsilon(q_c)(1 - \lambda_\epsilon) + \int_0^{\epsilon_m} \epsilon \lambda_\epsilon f_Q^t(g^{-1}(\epsilon) | q_m) \frac{dq}{d\epsilon} d\epsilon + \int_{\epsilon_m}^\infty \epsilon 0 d\epsilon, \tag{F11}$$

where  $\epsilon(q_c) = 0$ . This reduces to

$$\langle E \rangle = \lambda_\epsilon \int_0^{\epsilon_m} \epsilon f_Q^t(g^{-1}(\epsilon) | q_m) \frac{dq}{d\epsilon} d\epsilon. \tag{F12}$$

Note that up to this point, we have specified neither the form of  $f_{Q*}$  or  $\epsilon$ , which makes this approach general. This is also very similar to the approach of Tucker and Bras (2000), Lague et al. (2005), Huang and Niemann (2006b), and DiBiase and Whipple (2011) where they integrate over the magnitude of daily incision as a function of streamflow prorated by the probability of observing a particular streamflow magnitude

$$\langle E \rangle = \int_{q_c}^{q_m} \epsilon(q) f_Q(q) dq, \tag{F13}$$

except we have properly eliminated the probability of exceeding  $q_m$  and we keep explicit track of the effects of the erosion threshold and streamflow distribution on the frequency of erosion ( $\lambda_\epsilon$ ) and the magnitude of daily erosion (expressed by the pdf of  $\epsilon$ ).

The function  $g^{-1}(\epsilon)$  can be found from daily incision as a function of daily streamflow as derived by Lague et al. (2005)

$$\epsilon = K \langle Q \rangle^m S^n q_*^\gamma - \psi, \tag{F14}$$

where  $K$  is a complex erodibility coefficient,  $m$ ,  $n$ , and  $\gamma$  exponents defined in Lague et al. (2005) and  $\psi$  is the threshold of erosion. It can easily be shown  $\psi = K \langle Q \rangle^m S^n q_{c*}^\gamma$ , which, if we set  $\epsilon_o = K \langle Q \rangle^m S^n$  (a constant with respect to  $q$ ) reduces daily incision to

$$\epsilon = g(q) = \epsilon_o q_*^\gamma - \psi = \epsilon_o (q_*^\gamma - q_{c*}^\gamma), \tag{F15}$$

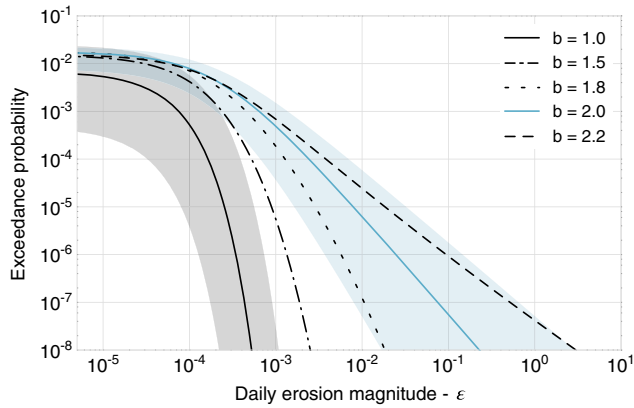


**Figure F1.** Distributions of daily erosion associated with the distributions of streamflow from Figure 3. For all distributions the ecohydrological and climatic conditions are held constant,  $\nu = 1$  and  $\gamma = 1$ . The shaded regions show the effect of changing the variability parameter from 0.5 to 2.0 for  $b = 1$  and  $b = 2$ .

where  $q_* = q/\mu$ . The inverse is then

$$g^{-1}(\varepsilon) = \left( \frac{\varepsilon + \psi}{\varepsilon_o \mu^{-\gamma}} \right)^{1/\gamma} \quad (\text{F16})$$

and then

$$\frac{dq}{d\varepsilon} = \frac{(\varepsilon + \psi)^{1/\gamma - 1}}{\gamma \varepsilon_o^{1/\gamma} \mu^{-1}}. \quad (\text{F17})$$

## F2. Distributions of Daily Erosion Rate

Recalling that

$$f_E(\varepsilon) = f_Q^t(g^{-1}(\varepsilon) | q_m) \frac{dq}{d\varepsilon}, \quad (\text{F18})$$

we arrive at the pdf of daily erosion by substituting equations (F16) and (F17) into (F18), choosing the appropriate form of  $f_Q^t(q)$  (equations (F1)–(F3)). For the case  $b = 1$

$$f_E(\varepsilon) = \frac{(\varepsilon + \psi)^{1/\gamma - 1}}{\eta \gamma (\varepsilon_o \nu^\gamma)^{1/\gamma}} \exp \left[ - \left( \frac{\varepsilon + \psi}{\varepsilon_o \nu^\gamma} \right)^{1/\gamma} \right], \quad (\text{F19})$$

where  $\eta = \Gamma(1/\nu)[\Gamma(1/\nu, q_{c^*}/\nu) - \Gamma(1/\nu, q_{m^*}/\nu)]$  is a normalizing constant that takes into account the fact that the distribution of erosion only exists for streamflows above  $q_{c^*}$  and below  $q_{m^*}$ . For  $b = 2$

$$f_E(\varepsilon) = \frac{(\varepsilon + \psi)^{-(1/\nu + 1)/\gamma - 1}}{\eta \gamma (\varepsilon_o \nu^{-\gamma})^{-(1/\nu + 1)/\gamma}} \exp \left[ - \left( \frac{\varepsilon + \psi}{\varepsilon_o \nu^{-\gamma}} \right)^{-1/\gamma} \right], \quad (\text{F20})$$

where  $\eta = \Gamma(1/\nu + 1)[\Gamma(1/\nu + 1, 1/\nu q_{m^*}) - \Gamma(1/\nu + 1, 1/\nu q_{c^*})]$  is a slightly different normalizing constant that serves the same role as in the case  $b = 1$ .

In the case  $b \neq 1, 2$

$$f_E(\varepsilon) = C_\varepsilon \frac{(\varepsilon + \psi)^{(1-b)/\gamma - 1}}{\varepsilon_o^{(1-b)/\gamma}} \exp \left[ - \frac{1}{\nu} \left( \frac{(\varepsilon + \psi)^{(2-b)/\gamma}}{(2-b)\varepsilon_o^{(2-b)/\gamma}} - \frac{(\varepsilon + \psi)^{(1-b)/\gamma}}{(1-b)\varepsilon_o^{(1-b)/\gamma}} \right) \right], \quad (\text{F21})$$

where  $C_\varepsilon$  is a normalizing constant such that  $\int_0^{\varepsilon_m} f_E(\varepsilon) d\varepsilon = 1$ . In the above expressions, we see that the pdf of daily erosion can be expressed as a function of geomorphic ( $K, S, m, n, \gamma, \psi$ ) and hydrological ( $b, \nu, \mu$ ) parameters.

Figure F1 shows the distributions of daily erosion corresponding to the distributions of daily streamflow in Figure 3. The effect of changing the variability index  $\nu$  is shown as shaded regions for  $b = 1$  and  $b = 2$ . Its influence is slightly different due to the significant probability to have days with no erosion at all.

## F3. Long-Term Erosion Rate

Before we solve the mean erosion intensity, it is useful to show two identities. First, we define a new variable  $\varepsilon_*$

$$\varepsilon_* = \frac{\varepsilon + \psi}{\varepsilon_o}. \quad (\text{F22})$$

If we substitute  $x$  into the pdf of daily erosion, where in the case  $b = 1$

$$x = k \varepsilon_*^{1/\gamma}, \quad (\text{F23})$$

it can be shown that

$$f_E(\varepsilon) = \frac{-x^{k-1}}{\eta} e^{-x} \quad (\text{F24})$$

and

$$k' \varepsilon_* f_E(\varepsilon) = \frac{-x^{k+\gamma-1}}{\eta} e^{-x}. \quad (\text{F25})$$

Similarly, in the case  $b = 2$ , if

$$x = k\varepsilon_*^{-1/\gamma}, \tag{F26}$$

then

$$f_E(\varepsilon) = \frac{-x^k}{\eta} e^{-x} \tag{F27}$$

and

$$k^{-\gamma} \varepsilon_* f_E(\varepsilon) = \frac{-x^{k-\gamma}}{\eta} e^{-x}. \tag{F28}$$

To solve for the mean erosion intensity in the case  $b = 1$

$$\bar{E} = \int_0^{\varepsilon_m} \varepsilon f_E^t(\varepsilon) d\varepsilon, \tag{F29}$$

we multiply by  $\varepsilon_o k^{-\gamma} / \varepsilon_o k^{-\gamma}$  and add and subtract the same term

$$\bar{E} = \varepsilon_o k^{-\gamma} \int_0^{\varepsilon_m} \frac{\varepsilon}{\varepsilon_o k^{-\gamma}} f_E^t(\varepsilon) d\varepsilon + \varepsilon_o k^{-\gamma} \int_0^{\varepsilon_m} \frac{\psi}{\varepsilon_o k^{-\gamma}} f_E^t(\varepsilon) d\varepsilon - \varepsilon_o k^{-\gamma} \int_0^{\varepsilon_m} \frac{\psi}{\varepsilon_o k^{-\gamma}} f_E^t(\varepsilon) d\varepsilon, \tag{F30}$$

which becomes

$$\bar{E} = \varepsilon_o k^{-\gamma} \int_0^{\varepsilon_m} k^\gamma \varepsilon_* f_E^t(\varepsilon) d\varepsilon - \psi \int_0^{\varepsilon_m} f_E^t(\varepsilon) d\varepsilon. \tag{F31}$$

Making use of our identities we can write

$$\bar{E} = \frac{-\varepsilon_o k^{-\gamma}}{\eta} \int_{x_c}^{x_m} x^{k+\gamma-1} e^{-x} dx - \frac{-\psi}{\eta} \int_{x_c}^{x_m} x^{k-1} e^{-x} dx, \tag{F32}$$

where  $x_c = kq_{c*}$  and  $x_m = kq_{m*}$ . We complete the solution using the following relationship derived from the definition of the incomplete gamma function

$$\int_\alpha^\beta x^{s-1} e^{-x} dx = \int_0^\beta x^{s-1} e^{-x} dx - \int_0^\alpha x^{s-1} e^{-x} dx = \Gamma(s) [\Gamma(s, \alpha) - \Gamma(s, \beta)]. \tag{F33}$$

Therefore, the analytical solution for the mean erosion intensity is

$$\bar{E} = \frac{\varepsilon_o k^{-\gamma} \Gamma(k + \gamma)}{\eta} [\Gamma(k + \gamma, kq_{c*}) - \Gamma(k + \gamma, kq_{m*})] - \frac{\psi \Gamma(k)}{\eta} [\Gamma(k, kq_{c*}) - \Gamma(k, kq_{m*})]. \tag{F34}$$

Recalling that  $\eta = \Gamma(k) [\Gamma(k, kq_{c*}) - \Gamma(k, kq_{m*})]$ , (F34) can be rewritten as

$$\bar{E} = \varepsilon_o \left[ \frac{\Gamma(k + \gamma)}{\Gamma(k) k^\gamma} \left( \frac{\Gamma(k + \gamma, kq_{c*}) - \Gamma(k + \gamma, kq_{m*})}{\Gamma(k, kq_{c*}) - \Gamma(k, kq_{m*})} \right) - q_{c*}^\gamma \right] = \varepsilon_o (\mu_\varepsilon / \lambda_\varepsilon - q_{c*}^\gamma). \tag{F35}$$

In the case the  $b = 2$ , we follow the same steps to find that

$$\begin{aligned} \bar{E} &= \frac{\varepsilon_o k^\gamma \Gamma(k + 1 - \gamma)}{\eta} [\Gamma(k + 1 - \gamma, k/q_{m*}) - \Gamma(k + 1 - \gamma, k/q_{c*})] \\ &\quad - \frac{\psi \Gamma(k + 1)}{\eta} [\Gamma(k + 1, k/q_{m*}) - \Gamma(k + 1, k/q_{c*})]. \end{aligned} \tag{F36}$$

Recalling again that here  $\eta = \Gamma(k + 1) [\Gamma(k + 1, k/q_{m*}) - \Gamma(k + 1, k/q_{c*})]$ , (F36) can be rewritten as

$$\bar{E} = \varepsilon_o \left[ \frac{\Gamma(k + 1 - \gamma)}{\Gamma(k) k^{1-\gamma}} \left( \frac{\Gamma(k + 1 - \gamma, k/q_{m*}) - \Gamma(k + 1 - \gamma, k/q_{c*})}{\Gamma(k + 1, k/q_{m*}) - \Gamma(k + 1, k/q_{c*})} \right) - q_{c*}^\gamma \right] = \varepsilon_o (\mu_\varepsilon / \lambda_\varepsilon - q_{c*}^\gamma). \tag{F37}$$

The mean long-term erosion rate is

$$\langle E \rangle = \lambda_\varepsilon \bar{E} = \mu_\varepsilon \varepsilon_o - \lambda_\varepsilon \psi. \tag{F38}$$

## Appendix G: Analytical Forms of $\mu_\epsilon$ and $\lambda_\epsilon$

For the case of  $b = 1$  and assuming  $q_{c^*} > 0$  and  $q_{m^*} < \infty$

$$\mu_\epsilon = \frac{\Gamma(1/\nu + \gamma)}{\Gamma(1/\nu)\nu^{-\gamma}} \left( \frac{\Gamma(1/\nu + \gamma, q_{c^*}/\nu) - \Gamma(1/\nu + \gamma, q_{m^*}/\nu)}{1 - \Gamma(1/\nu, q_{m^*}/\nu)} \right) \quad (G1)$$

$$\lambda_\epsilon = \frac{\Gamma(1/\nu, q_{c^*}/\nu) - \Gamma(1/\nu, q_{m^*}/\nu)}{1 - \Gamma(1/\nu, q_{m^*}/\nu)}. \quad (G2)$$

For the case of  $b = 2$  and again assuming  $q_{c^*} > 0$  and  $q_{m^*} < \infty$

$$\mu_\epsilon = \frac{\Gamma(1/\nu + 1 - \gamma)}{\Gamma(1/\nu)\nu^{\gamma-1}} \left( \frac{\Gamma(1/\nu + 1 - \gamma, 1/\nu q_{m^*}) - \Gamma(1/\nu + 1 - \gamma, 1/\nu q_{c^*})}{\Gamma(1/\nu + 1, 1/\nu q_{m^*})} \right) \quad (G3)$$

$$\lambda_\epsilon = \frac{\Gamma(1/\nu + 1, 1/\nu q_{m^*}) - \Gamma(1/\nu + 1, 1/\nu q_{c^*})}{\Gamma(1/\nu + 1, 1/\nu q_{m^*})}. \quad (G4)$$

The analytical solution for  $b = 1.5$  only applies when we can assume  $q_{m^*} \sim \infty$ .

### Acknowledgments

We thank Dimitri Lague for discussions and several thorough reviews which dramatically improved this article. In addition, we thank Kelin Whipple, Sally Thompson, and two anonymous reviewers for their time and thoughtful input which has also helped to shape this article. We also thank the Editor John Buffington and all Associate Editors involved for their time and thoughtful input. Finally, E. Deal and J. Braun express their thanks to the Earth and Planetary Science department at the University of California, Berkeley, who hosted them during part of the writing of this paper. The data used are listed in the references.

### References

- Acosta, V., Schildgen, T., Clarke, B., Scherler, D., Bookhagen, B., Wittmann, H., et al. (2015). Effect of vegetation cover on millennial-scale landscape denudation rates in East Africa. *Lithosphere*, 7(4), 408–420. <https://doi.org/10.1130/L402.1>
- Attal, M., Mudd, S., Hurst, M., Weinman, B., Yoo, K., & Naylor, M. (2015). Impact of change in erosion rate and landscape steepness on hillslope and fluvial sediments grain size in the Feather River Basin (Sierra Nevada, California). *Earth Surface Dynamics*, 3(1), 201–222.
- Bagnold, R. (1980). An empirical correlation of bedload transport rates in flumes and natural rivers. *Proceedings of the Royal Society of London A: Mathematical, Physical and Engineering Sciences*, 372, 453–473.
- Baker, V. R., & Kale, V. S. (1998). The role of extreme floods in shaping bedrock channels. In K. J. Tinkler & E. Wohl (Eds.), *Rivers over rock: Fluvial processes in bedrock channels* (pp. 153–165). Washington, DC: American Geophysical Union.
- Basso, S., Frascati, A., Marani, M., Schirmer, M., & Botter, G. (2015). Climatic and landscape controls on effective discharge. *Geophysical Research Letters*, 42, 8441–8447. <https://doi.org/10.1002/2015GL066014>
- Basso, S., Schirmer, M., & Botter, G. (2015). On the emergence of heavy-tailed streamflow distributions. *Advances in Water Resources*, 82, 98–110. <https://doi.org/10.1016/j.advwatres.2015.04.013>
- Beaumont, C., Fullsack, P., & Hamilton, J. (1992). Erosional control of active compressional orogens. In K. R. McClay (Ed.), *Thrust tectonics* (pp. 1–18). Surrey, England: Springer.
- Beer, A. R., & Turowski, J. (2015). Bedload transport controls bedrock erosion under sediment-starved conditions. *Earth Surface Dynamics*, 3(3), 291–309.
- Berghuijs, W., Hartmann, A., & Woods, R. (2016). Streamflow sensitivity to water storage changes across Europe. *Geophysical Research Letters*, 43, 1980–1987. <https://doi.org/10.1002/2016GL067927>
- Berghuijs, W. R., Sivapalan, M., Woods, R. A., & Savenije, H. H. (2014). Patterns of similarity of seasonal water balances: A window into streamflow variability over a range of time scales. *Water Resources Research*, 50, 5638–5661. <https://doi.org/10.1002/2014WR015692>
- Bermudez, M., Beek, P., & Bernet, M. (2012). Strong tectonic and weak climatic control on exhumation rates in the Venezuelan Andes. *Lithosphere*, 5(1), 3–16. <https://doi.org/10.1130/L212.1>
- Biswal, B., & Marani, M. (2010). Geomorphological origin of recession curves. *Geophysical Research Letters*, 37, L24403. <https://doi.org/10.1029/2010GL045415>
- Blanckenburg, F. (2005). The control mechanisms of erosion and weathering at basin scale from cosmogenic nuclides in river sediment. *Earth and Planetary Science Letters*, 237(3–4), 462–479. <https://doi.org/10.1016/j.epsl.2005.06.030>
- Bogaart, P. W., Velde, Y. v. d., Lyon, S. W., & Dekker, S. C. (2016). Streamflow recession patterns can help unravel the role of climate and humans in landscape co-evolution. *Hydrology and Earth System Sciences*, 20(4), 1413–1432. <https://doi.org/10.5194/hess-20-1413-2016>
- Botter, G. (2014). Flow regime shifts in the Little Piney Creek (US). *Advances in Water Resources*, 71, 44–54.
- Botter, G., Basso, S., Porporato, A., Rodriguez-Iturbe, I., & Rinaldo, A. (2010). Natural streamflow regime alterations: Damming of the Piave river basin (Italy). *Water Resources Research*, 46, W06522. <https://doi.org/10.1029/2009WR008523>
- Botter, G., Basso, S., Rodriguez-Iturbe, I., & Rinaldo, A. (2013). Resilience of river flow regimes. *Proceedings of the National Academy of Sciences*, 110(32), 12,925–12,930. <https://doi.org/10.1073/pnas.1311920110>
- Botter, G., Porporato, A., Rodriguez-Iturbe, I., & Rinaldo, A. (2007). Basin-scale soil moisture dynamics and the probabilistic characterization of carrier hydrologic flows: Slow, leaching-prone components of the hydrologic response. *Water Resources Research*, 43, W02417. <https://doi.org/10.1029/2006WR005043>
- Botter, G., Porporato, A., Rodriguez-Iturbe, I., & Rinaldo, A. (2009). Nonlinear storage-discharge relations and catchment streamflow regimes. *Water Resources Research*, 45, W10427. <https://doi.org/10.1029/2008WR007658>
- Budyko, M. (1974). *Climate and life, translated from Russian by D. H. Miller*. San Diego, CA: Academic.
- Burbank, D., Blythe, A., Putkonen, J., Pratt-Sitaula, B., Gabet, E., Oskin, M., et al. (2003). Decoupling of erosion and precipitation in the Himalayas. *Nature*, 426(6967), 652–655.
- Carretier, S., Regard, V., Vassallo, R., Aguilar, G., Martinod, J., Riquelme, R., et al. (2013). Slope and climate variability control of erosion in the Andes of central Chile. *Geology*, 41(2), 195–198.
- Ceola, S., Botter, G., Bertuzzo, E., Porporato, A., Rodriguez-Iturbe, I., & Rinaldo, A. (2010). Comparative study of ecohydrological streamflow probability distributions. *Water Resources Research*, 46, W09502. <https://doi.org/10.1029/2010WR009102>

- Chaudhry, M. A., Temme, N., & Veling, E. (1996). Asymptotics and closed form of a generalized incomplete gamma function. *Journal of Computational and Applied Mathematics*, 67(2), 371–379.
- Chen, B., & Krajewski, W. (2016). Analysing individual recession events: Sensitivity of parameter determination to the calculation procedure. *Hydrological Sciences Journal*, 61(16), 2887–2901.
- Collins, D., Bras, R., & Tucker, G. (2004). Modeling the effects of vegetation-erosion coupling on landscape evolution. *Journal of Geophysical Research*, 109, F03004. <https://doi.org/10.1029/2003JF000028>
- Crave, A., & Davy, P. (2001). A stochastic “precipiton” model for simulating erosion/sedimentation dynamics. *Computers and Geosciences*, 27(7), 815–827.
- Dahlen, F., & Suppe, J. (1988). Mechanics, growth, and erosion of mountain belts. *Geological Society of America Special Papers*, 218, 161–178.
- Daly, E., & Porporato, A. (2010). Effect of different jump distributions on the dynamics of jump processes. *Physical Review E*, 81(6), 061133. <https://doi.org/10.1103/PhysRevE.81.061133>
- Deal, E., Favre, A.-C., & Braun, J. (2017). Rainfall variability in the Himalayan orogen and its relevance to erosion processes. *Water Resources Research*, 53, 4004–4021. <https://doi.org/10.1002/2016WR020030>
- DiBiase, R. A., & Whipple, K. X. (2011). The influence of erosion thresholds and runoff variability on the relationships among topography, climate, and erosion rate. *Journal of Geophysical Research*, 116, F04036. <https://doi.org/10.1029/2011JF002095>
- DiBiase, R. A., Whipple, K. X., Heimsath, A. M., & Ouimet, W. B. (2010). Landscape form and millennial erosion rates in the San Gabriel mountains, CA. *Earth and Planetary Science Letters*, 289(1), 134–144.
- Doulatyari, B., Betterle, A., Basso, S., Biswal, B., Schirmer, M., & Botter, G. (2015). Predicting streamflow distributions and flow duration curves from landscape and climate. *Advances in Water Resources*, 83, 285–298. <https://doi.org/10.1016/j.advwatres.2015.06.013>
- Dralle, D. N., & Thompson, S. E. (2016). A minimal probabilistic model for soil moisture in seasonally dry climates. *Water Resources Research*, 52, 1507–1517. <https://doi.org/10.1002/2015WR017813>
- Dralle, D., Karst, N., & Thompson, S. (2015). A, B careful: The challenge of scale invariance for comparative analyses in power law models of the streamflow recession. *Geophysical Research Letters*, 42, 9285–9293. <https://doi.org/10.1002/2015GL066007>
- Feng, X., Porporato, A., & Rodriguez-Iturbe, I. (2015). Stochastic soil water balance under seasonal climates. *Proceedings of the Royal Society A: Mathematical, Physical and Engineering Sciences*, 471(2174), 20140623. <https://doi.org/10.1098/rspa.2014.0623>
- Ferrier, K., Huppert, K., & Perron, T. (2013). Climatic control of bedrock river incision. *Nature*, 496(7444), 206–9. <https://doi.org/10.1038/nature11982>
- Gentine, P., D’Odorico, P., Lintner, B. R., Sivandran, G., & Salvucci, G. (2012). Interdependence of climate, soil, and vegetation as constrained by the Budyko curve. *Geophysical Research Letters*, 39, L19404. <https://doi.org/10.1029/2012GL053492>
- Gilbert, G. K. (1877). *Report on the geology of the Henry Mountains* (170 pp.). US Geographical and Geological Survey of the Rocky Mountain Region, Government Printing Office.
- Godard, V., Bourlès, D., Spinabella, F., Burbank, D., Bookhagen, B., Fisher, B., et al. (2014). Dominance of tectonics over climate in Himalayan denudation. *Geology*, 42(3), 243–246. <https://doi.org/10.1130/G35342.1>
- Harman, C. J., Sivapalan, M., & Kumar, P. (2009). Power law catchment-scale recessions arising from heterogeneous linear small-scale dynamics. *Water Resources Research*, 45, W09404. <https://doi.org/10.1029/2008WR007392>
- Harris, F. E. (2008). Incomplete bessel, generalized incomplete gamma, or leaky aquifer functions. *Journal of Computational and Applied Mathematics*, 215(1), 260–269.
- Howard, A. D. (1994). A detachment-limited model of drainage basin evolution. *Water Resources Research*, 30(7), 2261–2285.
- Howard, A. D., Dietrich, W. E., & Seidl, M. (1994). Modeling fluvial erosion on regional to continental scales. *Journal of Geophysical Research*, 99, 13–13.
- Huang, X., & Niemann, J. (2006a). Modelling the potential impacts of groundwater hydrology on long-term drainage basin evolution. *Earth Surface Processes and Landforms*, 31(14), 1802–1823. <https://doi.org/10.1002/esp.1369>
- Huang, X., & Niemann, J. (2006b). An evaluation of the geomorphically effective event for fluvial processes over long periods. *Journal of Geophysical Research*, 111, F03015. <https://doi.org/10.1029/2006JF000477>
- Huang, X., & Niemann, J. D. (2008). How do streamflow generation mechanisms affect watershed hypsometry? *Earth Surface Processes and Landforms*, 33(5), 751–772.
- Ijjász-Vásquez, E. J., Bras, R. L., & Moglen, G. E. (1992). Sensitivity of a basin evolution model to the nature of runoff production and to initial conditions. *Water Resources Research*, 28(10), 2733–2741.
- Istanbulluoglu, E. (2009). An eco-hydro-geomorphic perspective to modeling the role of climate in catchment evolution. *Geography Compass*, 3(3), 1151–1175.
- Istanbulluoglu, E., & Bras, R. (2005). Vegetation-modulated landscape evolution: Effects of vegetation on landscape processes, drainage density, and topography. *Journal of Geophysical Research*, 110, F02012. <https://doi.org/10.1029/2004JF000249>
- Istanbulluoglu, E., & Bras, R. (2006). On the dynamics of soil moisture, vegetation, and erosion: Implications of climate variability and change. *Water Resources Research*, 42, W06418. <https://doi.org/10.1029/2005WR004113>
- Kirchner, J. (2009). Catchments as simple dynamical systems: Catchment characterization, rainfall-runoff modeling, and doing hydrology backward. *Water Resources Research*, 45, W02429. <https://doi.org/10.1029/2008WR006912>
- Lague, D. (2010). Reduction of long-term bedrock incision efficiency by short-term alluvial cover intermittency. *Journal of Geophysical Research*, 115, F02011. <https://doi.org/10.1029/2008JF001210>
- Lague, D. (2014). The stream power river incision model: Evidence, theory and beyond. *Earth Surface Processes and Landforms*, 39(1), 38–61. <https://doi.org/10.1002/esp.3462>
- Lague, D., Hovius, N., & Davy, P. (2005). Discharge, discharge variability, and the bedrock channel profile. *Journal of Geophysical Research*, 110, F04006. <https://doi.org/10.1029/2004JF000259>
- Laio, F., Porporato, A., Ridolfi, L., & Rodriguez-Iturbe, I. (2001). Plants in water-controlled ecosystems: Active role in hydrologic processes and response to water stress: II. Probabilistic soil moisture dynamics. *Advances in Water Resources*, 24(7), 707–723.
- Lamb, M. P., Dietrich, W. E., & Venditti, J. G. (2008). Is the critical shields stress for incipient sediment motion dependent on channel-bed slope? *Journal of Geophysical Research*, 113, F02008. <https://doi.org/10.1029/2007JF000831>
- Lehner, F., Wahl, E. R., Wood, A. W., Blatchford, D. B., & Llewellyn, D. (2017). Assessing recent declines in upper Rio Grande runoff efficiency from a paleoclimate perspective. *Geophysical Research Letters*, 44, 4124–4133. <https://doi.org/10.1002/2017GL073253>
- Milly, P. (1993). An analytic solution of the stochastic storage problem applicable to soil water. *Water Resources Research*, 29(11), 3755–3758. <https://doi.org/10.1029/93WR01934>
- Molnar, P., Anderson, R. S., Kier, G., & Rose, J. (2006). Relationships among probability distributions of stream discharges in floods, climate, bed load transport, and river incision. *Journal of Geophysical Research*, 111, F02001. <https://doi.org/10.1029/2005JF000310>

- Mueller, M. F., Dralle, D. N., & Thompson, S. E. (2014). Analytical model for flow duration curves in seasonally dry climates. *Water Resources Research*, 50, 5510–5531. <https://doi.org/10.1002/2014WR015301>
- Quimet, W. B., Whipple, K. X., & Granger, D. E. (2009). Beyond threshold hillslopes: Channel adjustment to base-level fall in tectonically active mountain ranges. *Geology*, 37(7), 579–582. <https://doi.org/10.1130/g30013a.1>
- Park, J., Botter, G., Jawitz, J., & Rao, P. (2014). Stochastic modeling of hydrologic variability of geographically isolated wetlands: Effects of hydro-climatic forcing and wetland bathymetry. *Advances in Water Resources*, 69, 38–48. <https://doi.org/10.1016/j.advwatres.2014.03.007>
- Porporato, A., D'odorico, P., Laio, F., Ridolfi, L., & Rodriguez-Iturbe, I. (2002). Ecohydrology of water-controlled ecosystems. *Advances in Water Resources*, 25(8), 1335–1348.
- Porporato, A., Daly, E., & Rodriguez-Iturbe, I. (2004). Soil water balance and ecosystem response to climate change. *The American Naturalist*, 164(5), 625–632.
- Riebe, C. S., Kirchner, J. W., Granger, D. E., & Finkel, R. C. (2001). Minimal climatic control on erosion rates in the Sierra Nevada, California. *Geology*, 29(5), 447–450.
- Rodriguez-Iturbe, I. (2000). Ecohydrology: A hydrologic perspective of climate-soil-vegetation dynamics. *Water Resources Research*, 36(1), 3–9.
- Rodriguez-Iturbe, I., Cox, D., & Isham, V. (1987). Some models for rainfall based on stochastic point processes. *Proceedings of the Royal Society A: Mathematical, Physical and Engineering Sciences*, 410(1839), 269–288. <https://doi.org/10.1098/rspa.1987.0039>
- Rodriguez-Iturbe, I., Isham, V., Cox, D. R., Manfreda, S., & Porporato, A. (2006). Space-time modeling of soil moisture: Stochastic rainfall forcing with heterogeneous vegetation. *Water Resources Research*, 42, W06D05. <https://doi.org/10.1029/2005WR004497>
- Rodriguez-Iturbe, I., Porporato, A., Ridolfi, L., Isham, V., & Cox, D. R. (1999). Probabilistic modelling of water balance at a point: The role of climate, soil and vegetation. *Proceedings of the Royal Society A: Mathematical, Physical and Engineering Sciences*, 455(1990), 3789–3805. <https://doi.org/10.1098/rspa.1999.0477>
- Roe, G. H., Montgomery, D. R., & Hallet, B. (2002). Effects of orographic precipitation variations on the concavity of steady-state river profiles. *Geology*, 30(2), 143–146.
- Rossi, M. W., Whipple, K. X., & Vivoni, E. R. (2016). Precipitation and evapotranspiration controls on daily runoff variability in the contiguous United States and Puerto Rico. *Journal of Geophysical Research: Earth Surface*, 121, 128–145. <https://doi.org/10.1002/2015JF003446>
- Rupp, D. E., & Selker, J. S. (2006). On the use of the boussinesq equation for interpreting recession hydrographs from sloping aquifers. *Water Resources Research*, 42, W12421. <https://doi.org/10.1029/2006WR005080>
- Schaeffli, B., Rinaldo, A., & Botter, G. (2013). Analytic probability distributions for snow-dominated streamflow. *Water Resources Research*, 49, 2701–2713. <https://doi.org/10.1002/wrcr.20234>
- Scherler, D., Bookhagen, B., & Strecker, M. R. (2014). Tectonic control on 10be-derived erosion rates in the Garhwal Himalaya, India. *Journal of Geophysical Research: Earth Surface*, 119, 83–105. <https://doi.org/10.1002/2013JF002955>
- Scherler, D., DiBiase, R. A., Fisher, G. B., & Avouac, J.-P. (2017). Testing monsoonal controls on bedrock river incision in the Himalaya and Eastern Tibet with a stochastic-threshold stream power model. *Journal of Geophysical Research: Earth Surface*, 122, 1389–1429. <https://doi.org/10.1002/2016JF004011>
- Settin, T., Botter, G., Rodriguez-Iturbe, I., & Rinaldo, A. (2007). Numerical studies on soil moisture distributions in heterogeneous catchments. *Water Resources Research*, 43, W05425. <https://doi.org/10.1029/2006WR005737>
- Shields, A. (1936). *Application of Similarity Principles and Turbulence Research to Bed-Load Movement (English translation by W. P. Ott and J. C. van Uchelen)*. USDA Soil Conservation Service, CalTech Hydrodynamics Laboratory Publication no. 167, 36 pp.
- Sklar, L. S., Riebe, C. S., Marshall, J. A., Genetti, J., Leclere, S., Lukens, C. L., et al. (2017). The problem of predicting the size distribution of sediment supplied by hillslopes to rivers. *Geomorphology*, 277, 31–49.
- Snyder, N. P., Whipple, K. X., Tucker, G. E., & Merritts, D. J. (2003). Importance of a stochastic distribution of floods and erosion thresholds in the bedrock river incision problem. *Journal of Geophysical Research*, 108(B2), 2117. <https://doi.org/10.1029/2001JB001655>
- Szilagyi, J., Gribovszki, Z., & Kalicz, P. (2007). Estimation of catchment-scale evapotranspiration from baseflow recession data: Numerical model and practical application results. *Journal of Hydrology*, 336(1-2), 206–217. <https://doi.org/10.1016/j.jhydrol.2007.01.004>
- Tague, C., & Grant, G. E. (2004). A geological framework for interpreting the low-flow regimes of Cascade streams, Willamette River Basin, Oregon. *Water Resources Research*, 40, W04303. <https://doi.org/10.1029/2003WR002629>
- Tamea, S., Muneeppeerakul, R., Laio, F., Ridolfi, L., & Rodriguez-Iturbe, I. (2010). Stochastic description of water table fluctuations in wetlands. *Geophysical Research Letters*, 37, L06403. <https://doi.org/10.1029/2009GL041633>
- Thompson, S. E., Harman, C. J., Troch, P. A., Brooks, P. D., & Sivapalan, M. (2011). Spatial scale dependence of ecohydrologically mediated water balance partitioning: A synthesis framework for catchment ecohydrology. *Water Resources Research*, 47, W00J03. <https://doi.org/10.1029/2010WR009998>
- Tucker, G., Lancaster, S., Gasparini, N., & Bras, R. (2001). The channel-hillslope integrated landscape development model (CHILD). *Landscape erosion and evolution modeling* (pp. 349–388). New York: Kluwer Academic/Plenum.
- Tucker, G. E. (2004). Drainage basin sensitivity to tectonic and climatic forcing: Implications of a stochastic model for the role of entrainment and erosion thresholds. *Earth Surface Processes and Landforms*, 29(2), 185–205. <https://doi.org/10.1002/esp.1020>
- Tucker, G. E., & Bras, R. L. (2000). A stochastic approach to modeling the role of rainfall variability in drainage basin evolution. *Water Resources Research*, 36(7), 1953–1964.
- Tucker, G. E., & Hancock, G. R. (2010). Modelling landscape evolution. *Earth Surface Processes and Landforms*, 35(1), 28–50. <https://doi.org/10.1002/esp.1952>
- Tucker, G. E., & Slingerland, R. L. (1994). Erosional dynamics, flexural isostasy, and long-lived escarpments: A numerical modeling study. *Journal of Geophysical Research*, 99(B6), 12,229–12,243.
- Veling, E. (2011). The generalized incomplete gamma function as sum over modified Bessel functions of the first kind. *Journal of Computational and Applied Mathematics*, 235(14), 4107–4116.
- Verma, P., Yeates, J., & Daly, E. (2011). A stochastic model describing the impact of daily rainfall depth distribution on the soil water balance. *Advances in Water Resources*, 34(8), 1039–1048. <https://doi.org/10.1016/j.advwatres.2011.05.013>
- Whipple, K., Hancock, G., & Anderson, R. (2000). River incision into bedrock: Mechanics and relative efficacy of plucking, abrasion, and cavitation. *Geological Society of America Bulletin*, 112(3), 490–503. [https://doi.org/10.1130/0016-7606\(2000\)112<490:RIIBMA>2.0.CO;2](https://doi.org/10.1130/0016-7606(2000)112<490:RIIBMA>2.0.CO;2)
- Whipple, K. X. (2009). The influence of climate on the tectonic evolution of mountain belts. *Nature Geoscience*, 2(2), 97–104. <https://doi.org/10.1038/ngeo413>
- Whipple, K. X., & Meade, B. J. (2006). Orogen response to changes in climatic and tectonic forcing. *Earth and Planetary Science Letters*, 243(1), 218–228.

- Whipple, K. X., & Tucker, G. E. (1999). Dynamics of the stream-power river incision model: Implications for height limits of mountain ranges, landscape response timescales, and research needs. *Journal of Geophysical Research*, *104*(B8), 17,661–17,674. <https://doi.org/10.1029/1999JB900120>
- Whipple, K. X., Kirby, E., & Brocklehurst, S. H. (1999). Geomorphic limits to climate-induced increases in topographic relief. *Nature*, *401*(6748), 39–43.
- Willett, S. D. (1999). Orogeny and orography The effects of erosion on the structure of mountain belts. *Journal of Geophysical Research*, *104*(B12), 28,957–28,981.
- Wobus, C., Whipple, K. X., Kirby, E., Snyder, N., Johnson, J., Spyropolou, K., et al. (2006). Tectonics from topography: Procedures, promise, and pitfalls. *Geological Society of America Special Papers*, *398*, 55–74. [https://doi.org/10.1130/2006.2398\(04\)](https://doi.org/10.1130/2006.2398(04))
- Wolman, G. M., & Miller, J. P. (1960). Magnitude and frequency of forces in geomorphic processes. *The Journal of Geology*, *68*(1), 54–74.
- Ye, S., Li, H. Y., Huang, M., Ali, M., Leng, G., Leung, L. R., et al. (2014). Regionalization of subsurface stormflow parameters of hydrologic models: Derivation from regional analysis of streamflow recession curves. *Journal of Hydrology*, *519*, 670–682.
- Yetemen, O., Istanbuluoglu, E., Flores-Cervantes, J. H., Vivoni, E. R., & Bras, R. L. (2015). Ecohydrologic role of solar radiation on landscape evolution. *Water Resources Research*, *51*, 1127–1157. <https://doi.org/10.1002/2014WR016169>
- Zhang, Y., Slingerland, R., & Duffy, C. (2016). Fully-coupled hydrologic processes for modeling landscape evolution. *Environmental Modelling & Software*, *82*, 89–107.